

Article

# Stratigraphic and Structural Control on Hydrothermal Dolomitization in the Middle Permian Carbonates, Southwestern Sichuan Basin (China)

Haofu Zheng <sup>1,2,3,\*</sup>, Yongsheng Ma <sup>1,2</sup>, Guoxiang Chi <sup>3</sup>, Hairuo Qing <sup>3</sup>, Bo Liu <sup>1,2,\*</sup>,  
Xuefeng Zhang <sup>1,2</sup> , Yingchu Shen <sup>1,2</sup>, Jianqiang Liu <sup>1,2</sup> and Yuanchong Wang <sup>1,2</sup>

<sup>1</sup> School of Earth and Space Sciences, Peking University, Beijing 100871, China; yongshenma@126.com (Y.M.); zhangxf@pku.edu.cn (X.Z.); ycshen@pku.edu.cn (Y.S.); liujq86@163.com (J.L.); wangyuanchong@pku.edu.cn (Y.W.)

<sup>2</sup> Institute of Oil & Gas, Peking University, Beijing 100871, China

<sup>3</sup> Department of Geology, University of Regina, Regina, SK S4S0A2, Canada; Guoxiang.Chi@uregina.ca (G.C.); Hairuo.Qing@uregina.ca (H.Q.)

\* Correspondence: zhenghaofu@pku.edu.cn (H.Z.); bobliu@pku.edu.cn (B.L.); Tel.: +86-010-62751150 (H.Z.); +86-010-62759360 (B.L.)

Received: 8 December 2018; Accepted: 5 January 2019; Published: 10 January 2019



**Abstract:** The Qixia Formation and Maokou Formation of Middle Permian in the southwestern Sichuan Basin were pervasively dolomitized during the diagenetic history. Petrographically, four types of dolomites, namely three replacive dolomites (Rd1, Rd2, and Rd3) and one dolomite cement (Cd), were distinguished. Rd1 dolomite occurs as very fine (<50 μm), planar-s to nonplanar crystals; Rd2 dolomite shows planar-e to planar-s crystal shapes with fine crystal sizes (50–250 μm) and is characterized by center-frog and margin-clear; Rd3 dolomite occurs as medium to coarse (250 μm–2 mm), nonplanar crystals; and Cd dolomite is characterized by saddle crystals filling dissolution pores and/or fractures, translucent white color in the hand samples, and strong sweeping extinction under cross-polarized light. In areas close to reactivated basement faults (Zhangcun outcrop and well Hanshen1), Rd3 (~65% by abundance) was the dominant type of replacement dolomite and minor amounts of Rd1 and Rd2 (~10%) were found in this area. Cd (~25%) was extensively developed in fractures and dissolution pores, whereas, in areas far away from the fault zones (Xinjigu outcrop), Rd1 (~20%) and Rd2 (~55%) were dominant replacement dolomites, and only a small portion of them were recrystallized to form Rd3 (~20%), with minor Cd (~5%) dolomite occurring in some dissolution pores. The  $\delta^{13}\text{C}_{\text{V-PDB}}$  (−0.37‰ to 4.32‰) and  $\delta^{18}\text{O}_{\text{V-PDB}}$  values (−7.41‰ to −5.19‰),  $^{87}\text{Sr}/^{86}\text{Sr}$  ratios (0.707085 to 0.707795), and rare earth elements (REE) patterns (flat REE patterns with slight light rare earth element (LREE) enrichment and slight negative Ce anomalies) suggest that Rd1 dolomite was formed penecontemporaneously in an evaporitic tidal flat evaporation environment with salinities higher than seawater. The Rd2 dolomite, characterized by  $\delta^{13}\text{C}_{\text{V-PDB}}$  (−0.18‰ to 4.89‰) and  $\delta^{18}\text{O}_{\text{V-PDB}}$  values from −6.6‰ to −5.5‰,  $^{87}\text{Sr}/^{86}\text{Sr}$  ratios from 0.707292 to 0.707951, and LREE enrichment and slight negative Ce anomalies, was interpreted as forming from the recrystallization of Rd1 at shallow burial. The  $\delta^{18}\text{O}_{\text{V-PDB}}$  values (−12.01‰ to −8.23‰), the prominent positive anomaly of Eu, high  $^{87}\text{Sr}/^{86}\text{Sr}$  ratios (0.7081–0.7198) and high fluid inclusion homogenization temperatures (149–255 °C) suggest that Rd3 and Cd dolomite were formed from hot fluids. Based on regional stratigraphic data, the Rd3 and Cd were likely formed at depths less than 1500 m; thus, the ambient burial temperature would be lower than 85 °C. The high fluid temperatures recorded by fluid inclusions, thus, indicate that the dolomitization was of hydrothermal nature. The  $\delta^{18}\text{O}_{\text{V-SMOW}}$  values, homogenization temperatures, and salinities of the fluid inclusions of Rd3 and Cd in proximal areas were systematically higher than those in distal areas, suggesting that the hydrothermal fluid ascended along faults in proximal areas and then migrated laterally along the strata to distal areas. The dolomites of the Middle Permian carbonates in the southwestern Sichuan

Basin, thus, resulted from different dolomitization phases, and the latter hydrothermal dolomitization was controlled by a combination of strata and structures.

**Keywords:** middle Permian; dolomite; hydrothermal dolomitization; petrology; geochemistry; control factor

---

## 1. Introduction

Hydrothermal dolomitization is considered as an important mechanism for the formation of massive dolostones in recent years [1–3]. Hydrothermal dolomitization attracted a great deal of attention because of the widespread distribution of deep-burial dolomites, which contain rich oil and natural gas resources [1,4–7]. Previous studies examined various factors controlling hydrothermal dolomitization and the genesis of different dolomites in hydrothermal activity areas [1,8–13]. However, the controlling factors on the distribution of different types of dolomites, including hydrothermal and non-hydrothermal ones, in a given area with hydrothermal activity, remain a subject in need of further study. Dolomitization in the Middle Permian southwestern Sichuan Basin is a good case to study the controlling factors of dolomitization in a hydrothermally active area.

The formation mechanisms and distribution patterns of the Middle Permian dolomites in the Sichuan Basin were controversial issues for decades. The present views include mixed-water dolomitization, burial dolomitization, basalt leaching-related dolomitization, and hydrothermal dolomitization [14–17]. Although it was suggested by many researchers that the Middle Permian dolomites were also formed due to hydrothermal activity related to tectonic movements [18–20], and the hydrothermal dolomite is spatially related to reactivated basement faults [18,19,21], the genesis of different types of dolomite and controlling factors of distribution between the dolomites near the fault (hereinafter called proximal areas) and those far away from the faults (hereinafter called distal areas) remain unclear.

In this study, we examined dolomite samples from the Middle Permian strata in the southwestern Sichuan Basin, both in areas proximal and distal to reactivated basement faults, to tackle the scientific problems discussed above. Specifically, we aimed to characterize the distribution of different types of dolomite in proximal and distal areas and to examine the factors that control such a distribution, which is important for evaluation of potential reservoirs in petroleum exploration. Detailed petrographic work was first carried out to characterize different types of dolomite and their timing relationship, followed by C–O–Sr isotopes and rare earth elements (REE) analyses of selected dolomite phases, which were used to evaluate the potential fluid source and thermal conditions of dolomitization. Fluid inclusion studies were then conducted on some of the dolomite phases to further constrain the dolomitization conditions. The results were compared between the proximal and distal areas, and a model linking dolomitization between the two areas was established. Finally, the significance of the study results for petroleum exploration and reservoir evaluation is discussed.

## 2. Geological Setting

The Sichuan Basin is located in southwestern China (Figure 1A). The Sichuan Basin is filled with marine sedimentary rocks from Precambrian to the Middle Triassic [22]. The basement of the Sichuan Basin is part of the Upper Yangtze Craton, and consists of crystalline rocks and meta-sedimentary rocks [23,24]. The Sichuan Basin is a composite superimposed craton basin with multiple tectonic cycles, including the Tongwan (Late Sinian), Caledonian (Cambrian to Silurian), Dongwu (Middle Permian), Indosinian (Middle to Late Triassic), Yanshanian (Late Triassic to Cretaceous), and Himalayan movements [1,25,26]. It is bound by the Emeishan–Liangshan fold belt in the southwest, Longmenshan fold belt in the northwest, and the Songpan–Ganzi, Qinling, and Dabashan fold belts in the north [27,28].

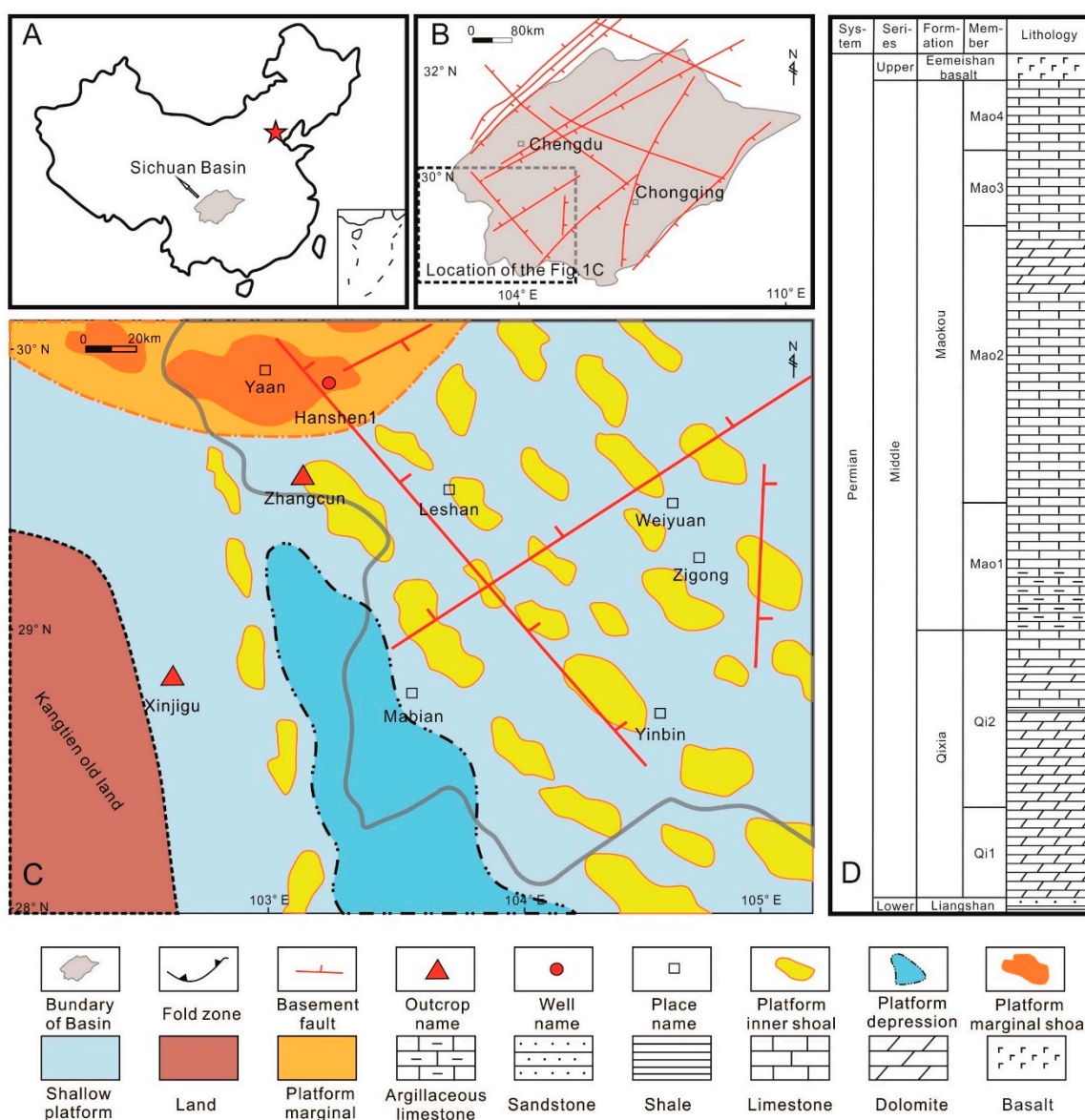


**Figure 1.** (A) Simplified location map of the Sichuan Basin. (B) Basement faults in the Sichuan Basin. (C) The location of study outcrops, wells, and sedimentary map of the Middle Permian (according to Zhou [29]). (D) Stratigraphic column of the Middle Permian in the southwest (SW) Sichuan Basin.

The Middle Permian in the Sichuan Basin is divided into two formations: the Qixia Formation and the Maokou Formation. The Qixia Formation was formed when the deposition environment evolved from an open platform during a transgressive systems tract into a rimmed platform associated with a highstand systems tract. The Maokou Formation was formed when the deposition environment evolved from a carbonate shelf during a highstand system tract into a rimmed platform [29].

The southwestern Sichuan Basin is generally in a shallow platform environment in Middle Permian (Figure 1C) [29]. The total thickness of the Qixia and Maokou formations is 270–363 m. The Qixia Formation is subdivided into two members (from bottom to top): Qi1 and Qi2 (Figure 1D), both consisting of mainly layered fine dolomite and medium-to-coarse dolomites. Micrite limestone is developed at the very top of the Qi2 member, consistent with a shallow-water platform depositional environment. The Maokou Formation is subdivided into four members: Mao1, Mao2, Mao3, and Mao4 from bottom to top. The Mao 1 member consists of micrite and argillaceous limestone, indicating a deep-water depositional environment. In contrast, the Mao2 and Mao3 members consist of bioclastic limestone and dolomite with sedimentary fabric (bioclastic) of precursor limestone preserved at the

very top of the Mao2 member, indicating high-frequency sea-level changes favorable for the deposition of grain shoals. The Mao4 member mainly consists of biomicrite and bioclastic limestone containing nodular chert, which is indicative of sea-level rises.

Many basement faults were developed inside and around the Sichuan Basin, which are clearly reflected in the aeromagnetic anomaly map [30]. There are two groups of basement structural lines, trending northeast (NE) and northwest (NW), respectively (Figure 1B). The activity of the basement faults in the Permian period is supported by stratigraphic, lithofacies, and tectonic evidence [30]. The burial history modeling of the Middle Permian strata of Well Hanshen1 (Figure 2) shows that, after deposition of the Permian, there was an uplift in the Variscan orogeny (Dongwu Movement), and the Maokou Formation suffered erosion of varying degrees due to uplifting related to the magmatic upwelling before the eruption of the Emeishan basalt (the thickness of the eroded layer is related to the distance from the Emeishan basalt) [31–33]. After a period of increasing burial during the Triassic, the Permian strata were uplifted again (but not exposed and eroded) during the Indosinian Movement in the latest Triassic, followed by increasing burial in Jurassic, Cretaceous, and Paleogene until the Neogene (the Himalayan Orogeny), when the strata were uplifted again. The maximum depth of burial experienced by the Permian in the western Sichuan Basin is approximately 7000 m [31–33].

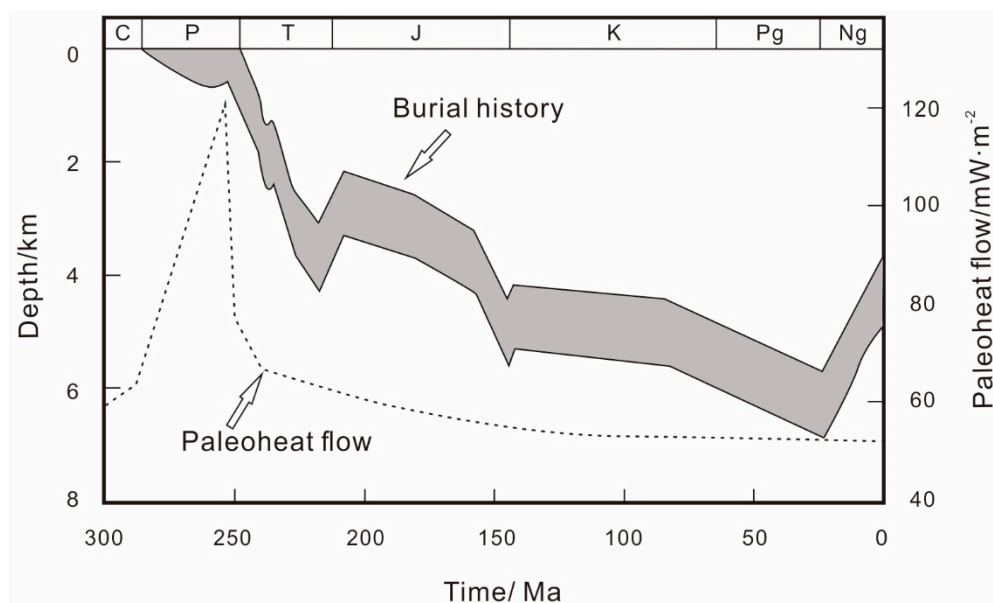


**Figure 2.** The synthetic map of burial history–paleoheat flow distribution of Well Hanshen1 in the southwest Sichuan Basin [31–33].

### 3. Samples and Study Methods

More than 100 dolomite, limestone, and calcite vein samples were collected from the Xinjigu field outcrop (XJG) (length of the section was 270 m), Zhangcun (ZC) field outcrop (length of the section was 300 m), and Well Hanshen1 (HS1) (length of the cores was 33 m). Detailed field and drill core observations were carried out and macroscopic characteristics of the samples were documented. Most of the dolomite samples were collected from the Qixia Formation at XJG, ZC, and well HS, while a few dolomite samples were collected from the Maokou Formation (Mao2 Member) at XJG. Limestone samples were collected from both the Qixia and Maokou formations. Subsequently, petrographic study on thin sections of more than 100 selected samples was carried out at the Institute of Oil and Gas, the School of Earth and Space Sciences, Peking University. The thin sections were stained with Alizarin Red S to distinguish calcite from dolomite [34]. Then, selected polished thin sections of dolomite and limestone samples were examined with a scanning electron microscope (SEM), using a

FEI-QUANTA650FEG (Thermo Fisher Scientific, Waltham, MA, USA) with a working current of 10 kV and a working distance of 11.4 mm.

All geochemical analyses were conducted at Peking University. For the analysis of trace elements and REEs, 60 mg of sample powder was digested with 0.5 mL of HNO<sub>3</sub> (1 + 1) and then dried. Then, 5 mL of HNO<sub>3</sub> (1.42 g/mL) was added to the dried sample and heated at 130 °C for 3 h. Finally, the solution was diluted with ultrapure H<sub>2</sub>O to a volume of 50 mL for trace element analysis. An inductively coupled plasma mass spectrometer (ICP-MS) was used to determine the trace element, including rare earth element contents, in the Key Laboratory of Orogenic Belts and Crustal Evolution at Peking University. The post-Archean average shale (PAAS) [35] was used to normalize the REE pattern. Eu and Ce anomaly values were calculated as follows:  $Eu/Eu^* = Eu_{SN} / (0.67Sm_{SN} + 0.33Tb_{SN})$ , and  $Ce/Ce^* = Ce_{SN} / (0.5La_{SN} + 0.5Pr_{SN})$  [36].

For carbon and oxygen isotopic analysis, powdered samples were reacted with 99% H<sub>3</sub>PO<sub>4</sub> at 75 °C for 16 h at the School of Archaeology and Museology in Peking University using an IsoPrime 100 instrument. The standard used for this analysis was IAEA CO-8 Calcite, and the analytical precision was ± 0.1‰ for both δ<sup>13</sup>C and δ<sup>18</sup>O values. All results were reported with reference to the Vienna Pee Dee Belemnite (VPDB) standard. The δ<sup>13</sup>C values of the fluid were calculated using Golyshev's (1981) [37] equilibrium carbon isotope fractionation equation ( $10^3 \ln \alpha_{\text{dolomite-fluid}} = 0.0758 \times 10^{18} T^{-6} - 5.767 \times 10^{12} T^{-4} + 31.3743 \times 10^9 T^{-3} - 62.581 \times 10^6 T^{-2} + 49.208 \times 10^3 T^{-1} - 11.393$ ), and the δ<sup>18</sup>O values of the fluid were calculated using Zheng's (1999) [38] equilibrium oxygen isotope fractionation equation ( $10^3 \ln \alpha_{\text{dolomite-fluid}} = 4.06 \times 10^6 T^{-2} - 4.65 \times 10^3 T^{-1} + 1.71$ ). The conversion of δ<sup>18</sup>O (VPDB) to δ<sup>18</sup>O (VSMOW) was performed using  $\delta^{18}O \text{ (VPDB)} = 1.03091 \times \delta^{18}O \text{ (VSMOW)} - 30.91$  [39].

For strontium isotope analysis, 120 mg of sample powder was dissolved in 2.5 mol/L HCl. Then, strontium was further separated by conventional cation exchange procedures utilizing ion exchange resin. The strontium isotope analyses were performed using a TRITON mass spectrometer and corrected relative to the NBS987 standard [40]; the mean error was ±1.0 × 10<sup>-5</sup> (2σ).

The fluid inclusion microthermometry was performed at the Geofluids Lab, University of Regina. Homogenization temperatures (T<sub>h</sub>) and final melting temperatures (T<sub>m-ice</sub>) were for two-phase aqueous inclusions in double-polished (100 μm thick) sections using a Linkam THMGS600 heating–freezing stage. The stage was calibrated with synthetic fluid inclusions, and the precision was ±1 °C for T<sub>h</sub> and ±0.1 °C for T<sub>m-ice</sub>.

The concept of the fluid inclusion assemblage (FIA) [41] was used to guide our fluid inclusion measurement and data analysis. Although it was difficult to be certain that there were fluid inclusions in our samples, typically randomly distributed, they may be accurately assigned to individual FIAs. The consistency of fluid inclusion data within a small area in a crystal can still be a constraint on the validity of the data [42]. In this study, a group of randomly distributed fluid inclusions in a microdomain, defined as an area >1 mm × 1 mm in one crystal, were treated like an FIA (even though it is not really an FIA according to the Goldstein and Reynolds 1994 definition). The fluid inclusion data were considered to be (a) “consistent”, when the T<sub>h</sub> variation of fluid inclusions in a microdomain with variable sizes and shapes was <10 °C; (b) “moderately consistent”, when the T<sub>h</sub> variation was between 10 °C and 15 °C; or (c) “inconsistent”, when the T<sub>h</sub> variation was >15 °C. The “moderately consistent” and “inconsistent” data were considered to reflect either inhomogeneous trapping or significant post-trapping modification and were not adopted for thermal history interpretation. The “consistent” data were interpreted to reflect homogeneous trapping and negligible post-trapping modification and were generally adopted. However, if the lower range of the “consistent” T<sub>h</sub> values was significantly higher than those of the “moderately consistent” and “consistent” T<sub>h</sub> values within the same sample, then even the “consistent” data were not adopted because they may have also experienced some degree of post-trapping modification despite the consistency of the data. The bulk salinities and NaCl/(NaCl + CaCl<sub>2</sub>) molar ratios (R<sub>NaCl</sub>) were calculated with T<sub>m-ice</sub> using the program by Steele–MacInnis et al. (2011) [43]. Since we were unable to measure hydrohalite melting temperatures (T<sub>m-HH</sub>) in this study due to low visibility, the calculated R<sub>NaCl</sub> represents the maximum value as explained in Chi (2007) [44].

## 4. Results

### 4.1. Petrography and Paragenesis

In areas proximal and distal to the basement faults, outcrop and hand specimen observations showed different compositions and structural features of dolomite. In distal areas (approximately 60 km from the nearest basement fault) (Figure 1C), dolomites were dominantly of replacement origin and fine-grained, with minor dolomite cements occurring in some dissolution pores (Figure 3A,B), whereas, in proximal areas, replacement dolomites were relatively coarse and dolomite cements were extensively developed in fractures and dissolution pores (Figure 3C,D).

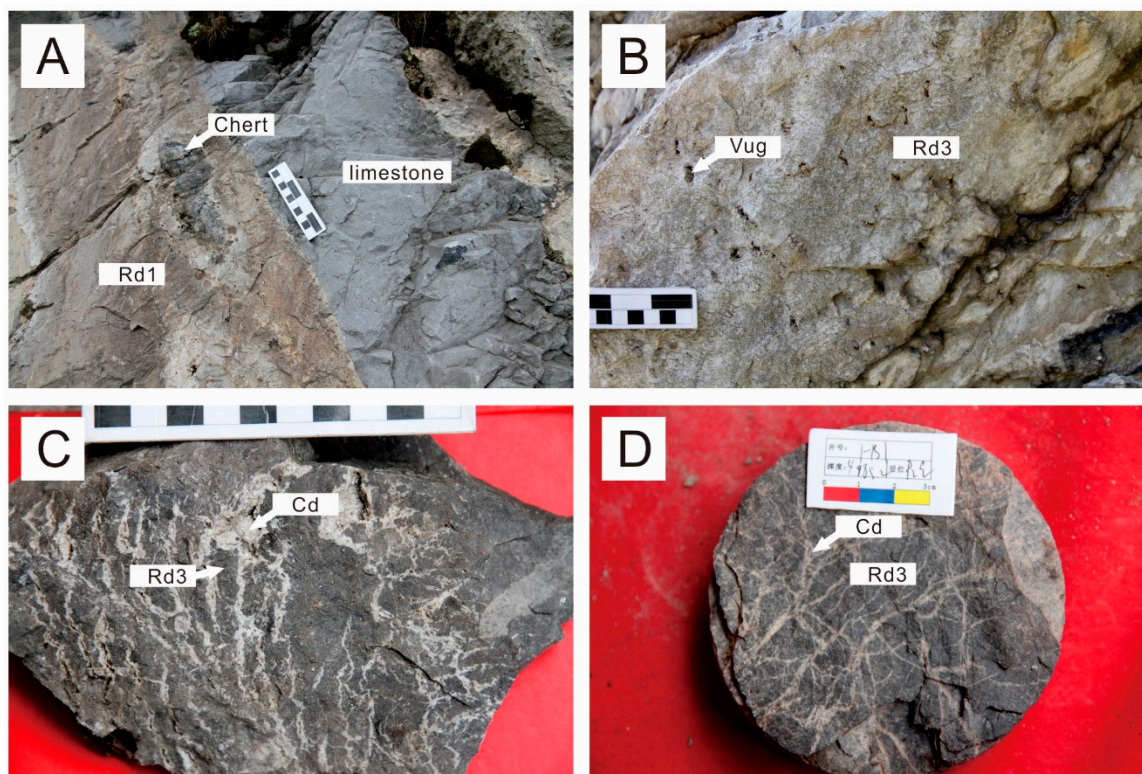


**Figure 3.** Field and core photos. (A) Field photo (Xinjigu;  $P_{2m}$ ) showing micritic dolomite (Rd1) has the characteristics of stratified development with chert; (B) field photo (Xinjigu;  $P_{2q}$ ) showing dissolved vugs developed in replacive dolomite; (C) field photo (Zhangcun;  $P_{2q}$ ) showing zebra fabrics developed in dolomitized host rock (medium-to-coarse dolomite, Rd3), fractures are filled by white dolomite cement (Cd); (D) core photo showing dissolved vugs and network fractures developed in dolomite which are filled by white dolomite cements (Cd) (4985.2 m, Well Hanshen1;  $P_{2q}$ ).

The dolomite was divided into two basic types, replacement dolomite (Rd) and cement dolomite (Cd). The replacement dolomite was further divided into three types, Rd1, Rd2, and Rd3. In addition to dolomite, halite, fluorite, quartz, siderite, and bitumen were in the samples examined. The petrographic characteristics of different dolomite phases and other minerals are described below.

The Rd1 dolomite was mainly developed at the bottom of the Qi1 member and the upper Mao2 member in distal areas (~20% by abundance) and commonly consisted of dolomicrite to tightly packed micritic crystals (< 50  $\mu\text{m}$ ) displaying planar-s to nonplanar-a texture with laminar fabric (Figure 4A). The sedimentary fabrics of precursor limestones (Figure 4G,H) (mimic replacement) were preserved in Rd1 dolomite, and early-phase dissolution vugs were developed between the particles and were filled with quartz cements (Figure 4B,E,F). In the cathodoluminescence images, Rd1 displayed dull luminescence, but locally (bioclasts and part of their rims) showed relatively bright-red luminescence (Figure 4C,D).

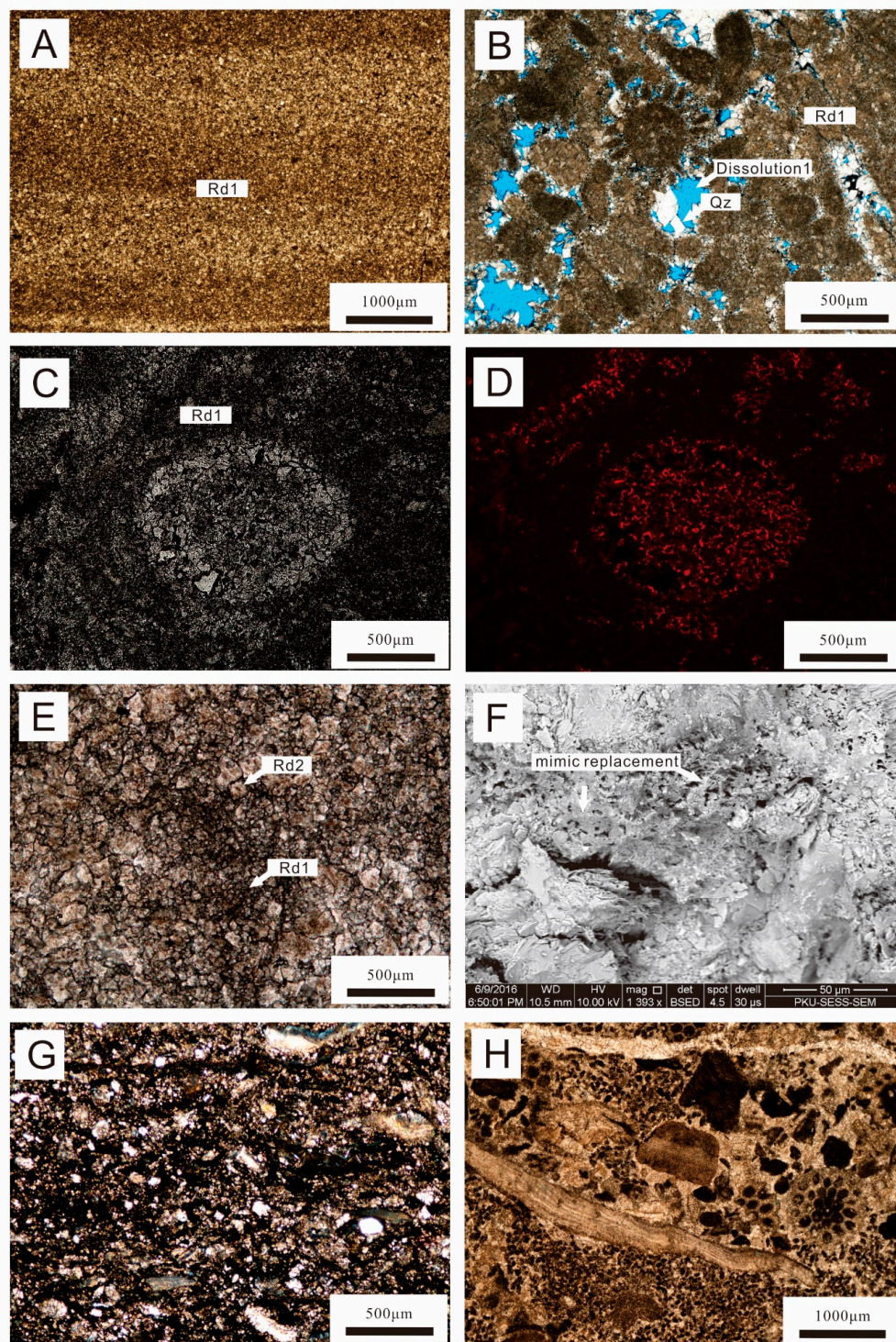


**Figure 4.** Rd1 dolomite. (A) Micritic replacive dolomite (Rd1) with laminar fabric (Xinjigu;  $P_{2q}$ ); (B) Rd1 with residual particles mimics replacement and early-phase dissolution vugs (Dissolution1) developed between the particles and later filled with quartz cements (Qz) (Xinjigu;  $P_{2m}$ ); (C) Rd1 with residual texture (Xinjigu;  $P_{2m}$ ); (D) cathodoluminescence (CL) photomicrograph of (C) exhibiting Rd1 displaying dull luminescence but bright-red thin rims in residual texture; (E) euhedral to subhedral Rd2 dolomite crystals were recrystallized from Rd1 dolomite, showing different sizes and shapes (Xinjigu;  $P_{2q}$ ); (F) photomicrograph (SEM) of residual texture (Xinjigu;  $P_{2m}$ ); (G) photomicrograph of argillaceous limestone (Xinjigu;  $P_{2q}$ ); (H) photomicrograph of bioclast limestone (Xinjigu;  $P_{2m}$ ).

The Rd2 dolomite was mainly developed in distal areas in the upper Q1 member, Q2 member, and upper Mao2 member (~55% by abundance), and minor Rd2 dolomite occurred in proximal areas at the bottom of the Qi member (~10% by abundance). The Rd2 dolomite commonly consisted of planar euhedral to subhedral crystals (50–250  $\mu\text{m}$ ) and was cut by stylolite (Figure 5A). The sedimentary fabrics were not preserved in Rd2, and the Rd2 dolomite was partially recrystallized to Rd3 dolomite (Figure 5B). Euhedral to subhedral crystals had a cloudy core surrounded by a clear rim (Figure 5C). Under cathodoluminescence (CL) light, Rd2 dolomite displayed very dull luminescence, while the crystals close to vugs showed bright-red rims (Figure 5D). Under a scanning electron microscope, it was noticeable that Rd2 dolomite crystals became coarser near the vugs (Figure 5E,F).

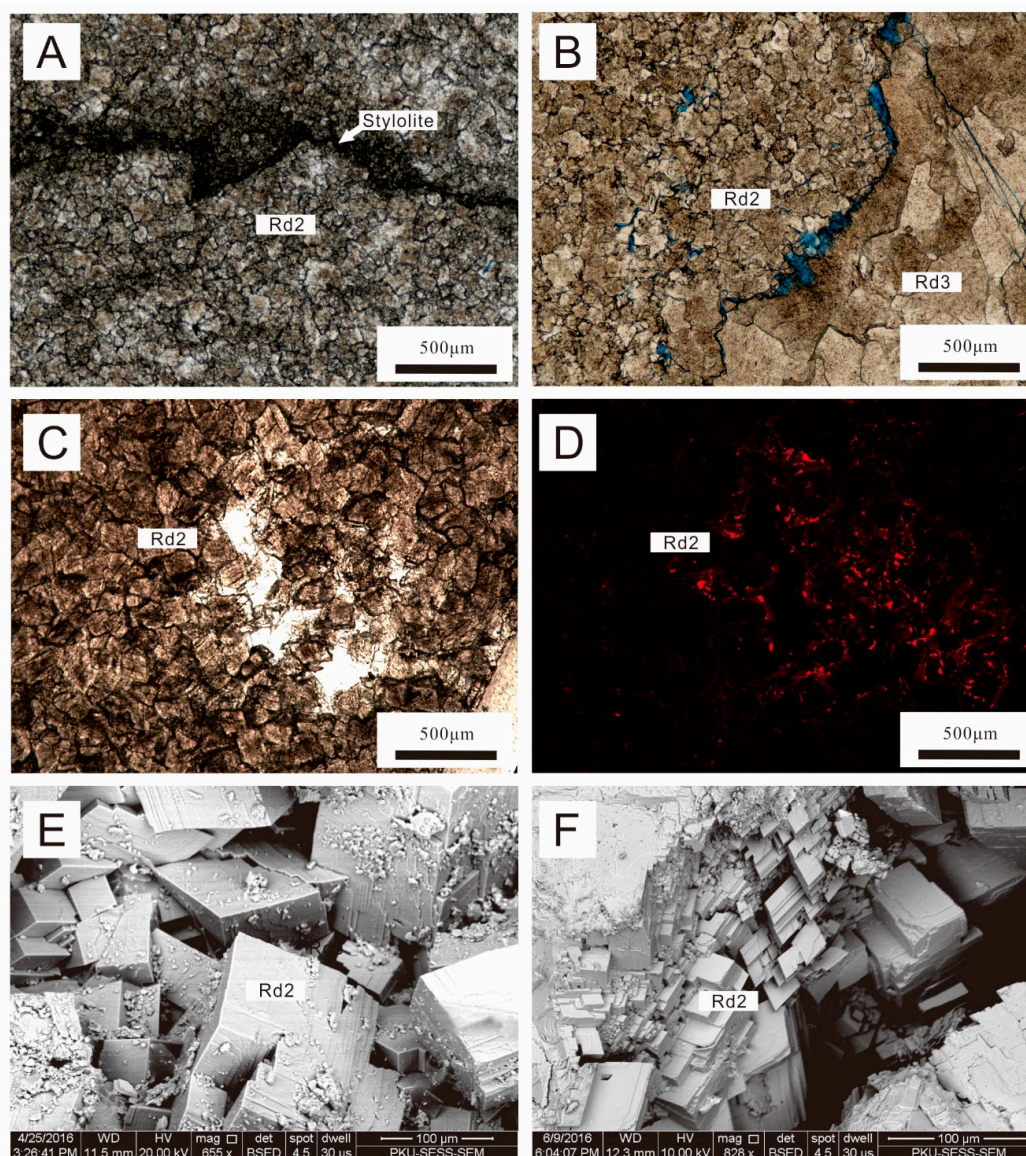


**Figure 5.** Rd2 dolomite. (A) Photomicrograph of planar euhedral to subhedral Rd2 dolomite crystals cut by stylolite (Xinjigu;  $P_{2q}$ ); (B) portion of euhedral to subhedral Rd2 dolomite recrystallized to Rd3 dolomite with curved crystals, showing different sizes and shapes (Xinjigu;  $P_{2q}$ ); (C) euhedral to subhedral crystals had a cloudy core surrounded by a clear rim (Xinjigu;  $P_{2m}$ ); (D) cathodoluminescence (CL) photomicrograph of (C) exhibiting Rd2 dolomite displayed very dull luminescence, but the crystals close to vugs showed bright-red rims (Xinjigu;  $P_{2m}$ ); (E,F) photomicrograph (SEM) exhibiting fine Rd2 dolomite crystals showing coarser crystals in vugs (Xinjigu;  $P_{2q}$ ).

Most of the Rd3 dolomites were developed in proximal areas in the Qi and Q2 members (~65% by abundance), while a small amount (~20% by abundance) of Rd3 was developed in distal areas at the top of the Qi1 member and the bottom of the Q2 member. The crystals were nonplanar, about 250 mm to 2 mm in size, and were cut by burial stylolite and intercrystalline pores preserved in Rd3 dolomite (Figure 6A,C,D). In the intercrystalline pores of Rd3 dolomite, quartz cement and bitumen were developed (Figure 6B). Calcite cements in fractures cross-cut the quartz cement and Rd3 dolomite, which were cross-cut by later fractures associated with dissolution (Figure 6C). Under cathodoluminescence light, Rd3 dolomite showed dull-red luminescence, with zones of very dull luminescence toward the rims (Figure 6E,F).

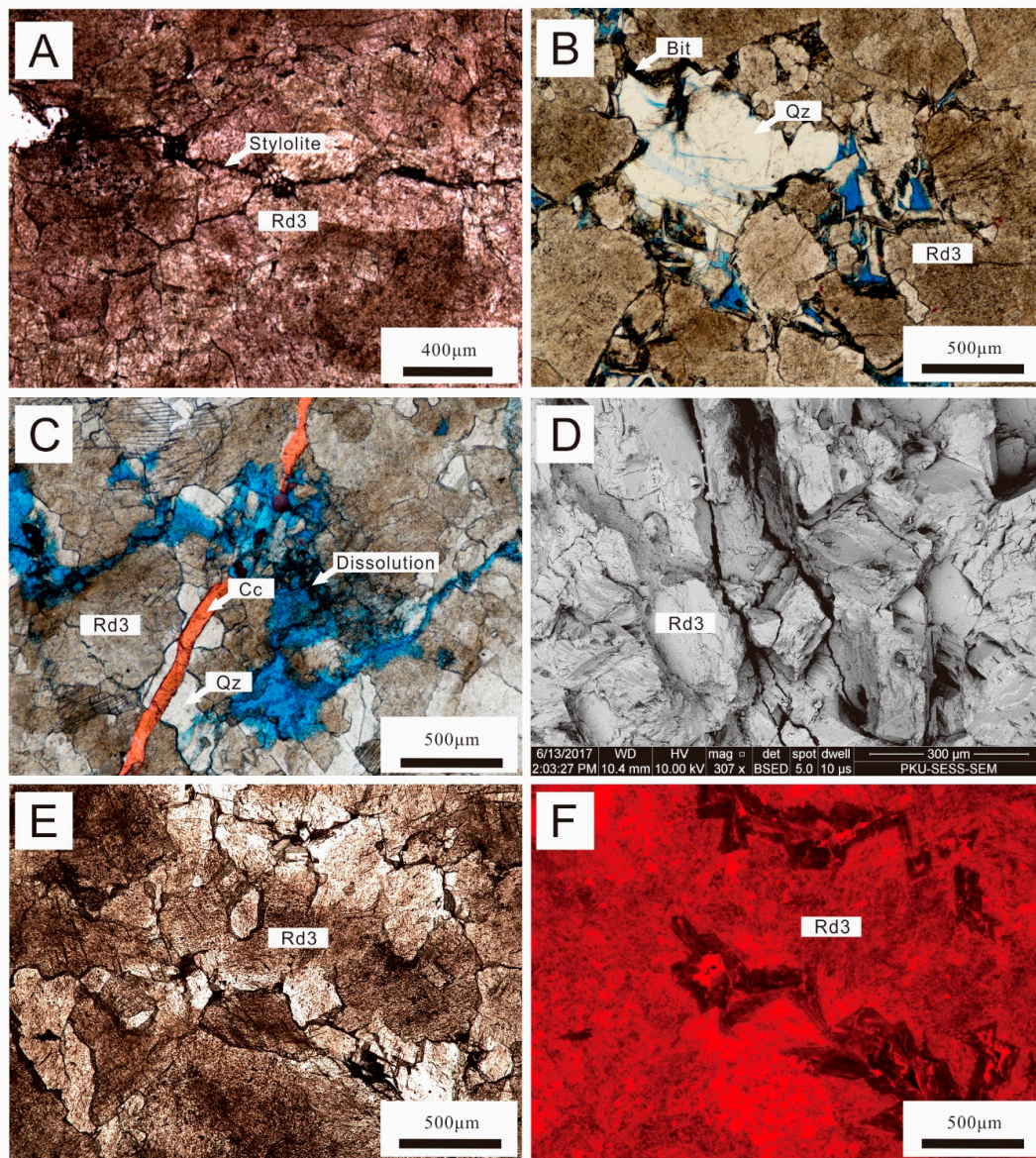


**Figure 6.** Rd3 dolomite. (A) Burial stylolite cross-cutting Rd3 (Well Hanshen1; P<sub>2q</sub>); (B) quartz (Qz) in the intercrystalline pores of Rd3 dolomite with bitumen (Bit) (Xinjigu; P<sub>2q</sub>); (C) calcite cements (Cc) in fracture (Fx) cross-cutting Qz and Rd3, with late-phase dissolved Fx cross-cutting Qz, Rd3, and Cc (Zhangcun; P<sub>2q</sub>); (D) photomicrograph of coarse and curved crystals of Rd3 dolomite (SEM) (4988.5 m; Well Hanshen1; P<sub>2q</sub>); (E,F) paired photomicrographs of medium-to-coarse crystalline, nonplanar-a dolomite. Rd3 dolomite shows strong dull-red luminescence under CL (Zhangcun; P<sub>2q</sub>).

Zebra fabrics in replacement dolomite (Rd) and hydraulic fractures were filled by white dolomite cement (Cd), and were well developed in proximal areas (~25% by abundance) in the Qi1 and Qi2 members. In contrast, Cd dolomite only appeared as a void-filling mineral in the host Rd dolomite in distal areas (~5% by abundance) at the top of the Qi1 member and the bottom of the Q2 member. The saddle Cd dolomite crystals showed a strong sweeping extinction under cross-polarized light and the residual pores were filled by later calcite cementation (Figure 7B). Cd dolomite exhibited dull-red luminescence with a rim characterized by bright CL zonation, while void-filling calcite showed non-luminescence (Figure 7C–F).

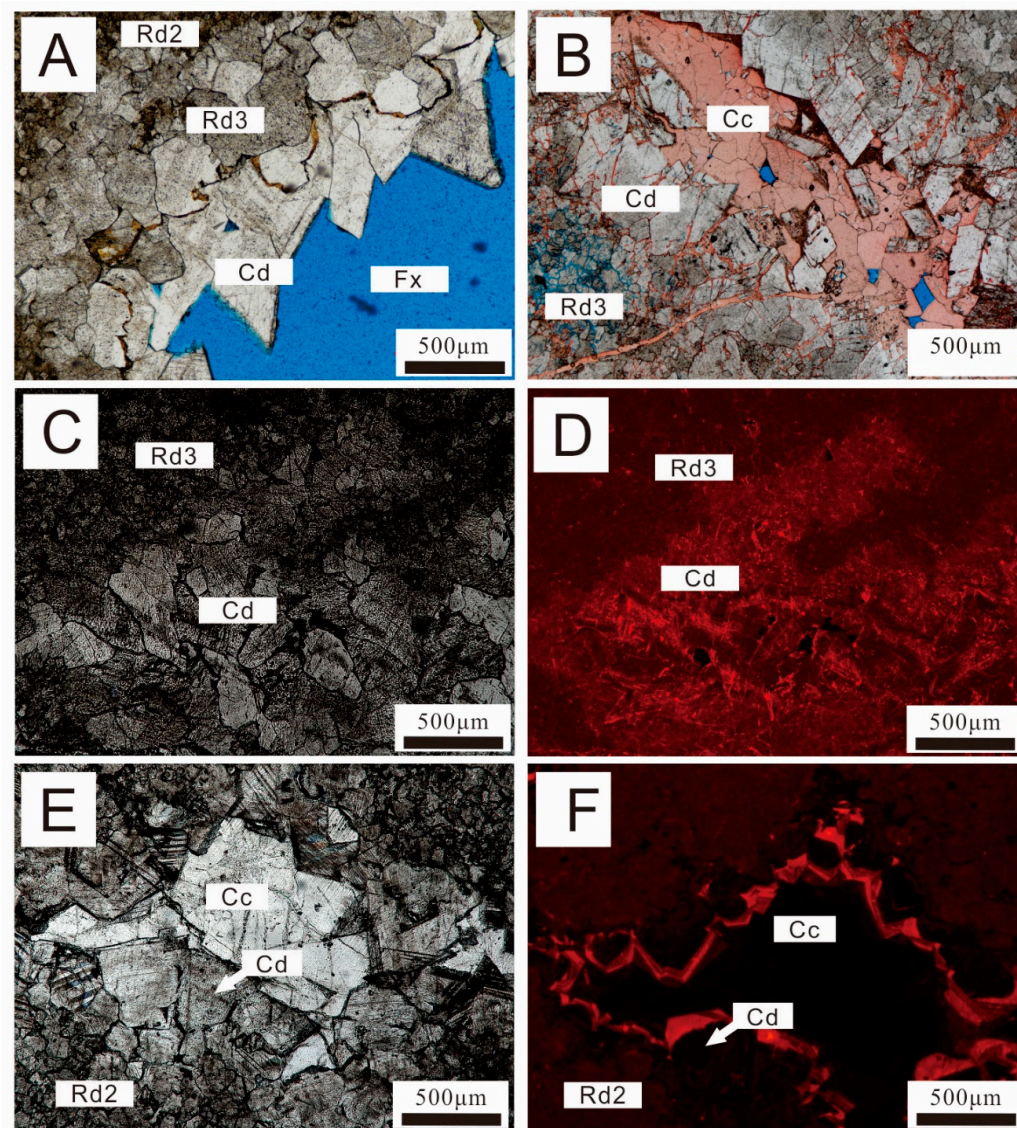


**Figure 7.** Cd dolomite. (A) Photomicrograph showing Cd dolomite filling in the hydraulic fractures (Fx), close to the matrix Rd3 dolomite and fine crystal dolomite (Rd2); (B) photomicrograph of void-filling Cd dolomite coarse-textured crystal aggregates and the residual porosity filled by later calcite (Cc) (Frac./Vug Cal) (Zhangcun; P<sub>2q</sub>); (C,D) paired photomicrographs (CL) of void-filling Cd dolomite and host Rd3 dolomite. Both Rd3 dolomite and Cd dolomite show strong dull-red luminescence and Cd dolomite exhibits mottled luminescence (Zhangcun; P<sub>2q</sub>); (E,F) paired photomicrographs (CL) of void-filling Cd dolomite, void-filling calcites, and host Rd2 dolomite. Rd2 dolomite shows dull-red luminescence and Cd dolomite shows bright-red rims with non-luminescence of calcites (Xinjigu; P<sub>2q</sub>).

Pyrite was the most common sulfide mineral to precipitate after Rd3 and Cd dolomite (Figure 8A). SEM energy-dispersive X-ray spectroscopy (EDS) analyses also demonstrated the existence of halite, fluorite, quartz, siderite, and bitumen in the interstitial spaces between dolomite; these minerals represented the last diagenetic phases in the paragenetic sequence (Figure 8B–F).

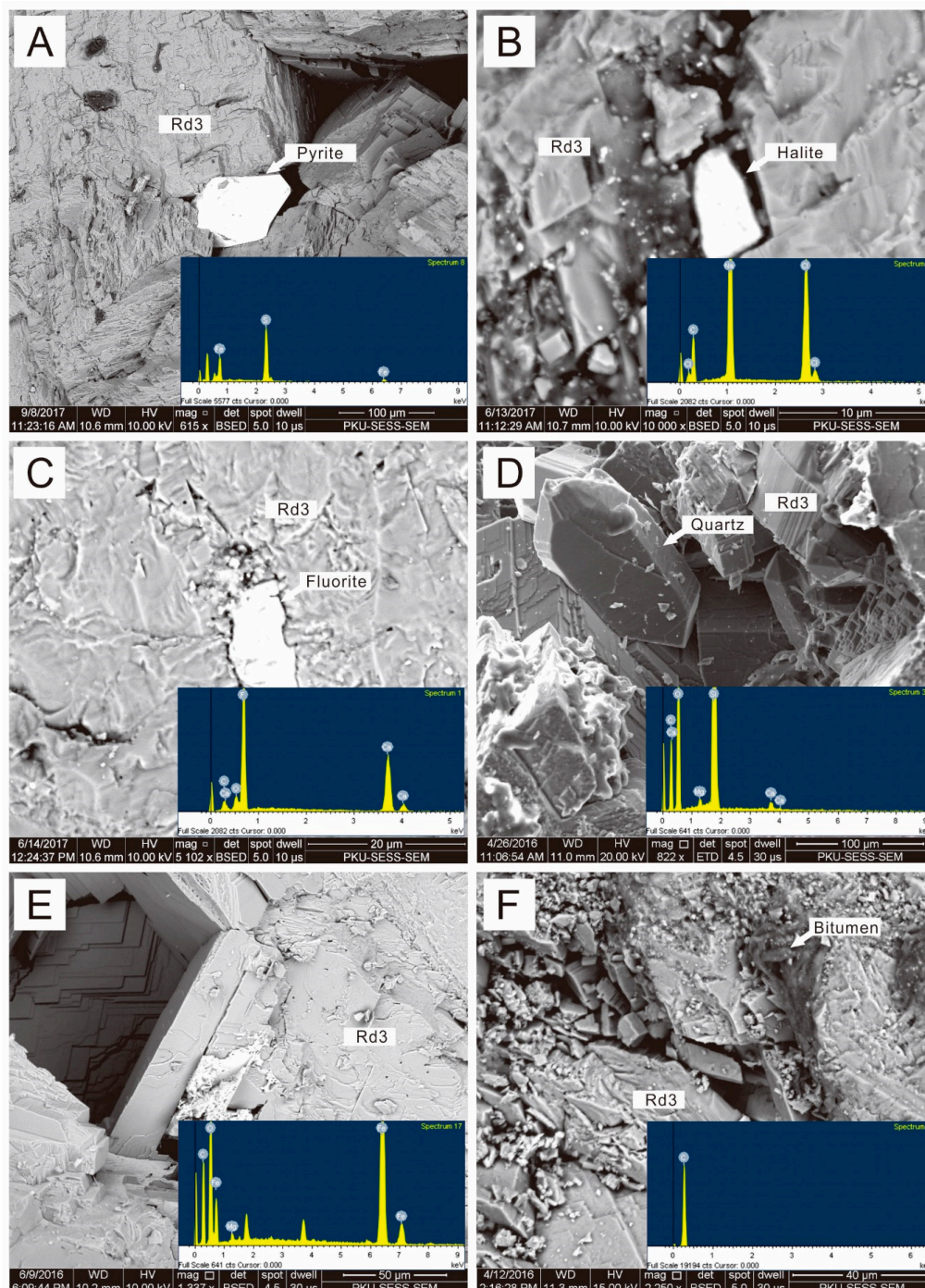


**Figure 8.** SEM images and energy-dispersive X-ray spectroscopy (EDS) analysis images of intercrystalline minerals in Rd3 and Cd dolomites. (A) Pyrite crystals within intercrystalline pores (4966 m; Well Hanshen1; P<sub>2q</sub>); (B) halite crystals within intercrystalline pores (4971.6 m; Well Hanshen1; P<sub>2q</sub>); (C) fluorite crystals within intercrystalline pores (4992 m; Well Hanshen1; P<sub>2q</sub>); (D) quartz crystals within intercrystalline pores (Xinjigu; P<sub>2q</sub>); (E) siderite crystals within intercrystalline pores (Xinjigu; P<sub>2q</sub>); (F) bitumen crystals within intercrystalline pores (Zhangcun; P<sub>2q</sub>).

#### 4.2. Fluid Inclusion Studies

No workable fluid inclusions were found in Rd1 and Rd2 due to small sizes of the crystals. Fluid inclusions were studied in replacement dolomite Rd3, cement dolomite (Cd), and calcite cements (Cc). The fluid inclusions consisted of a liquid phase and a vapor phase at room temperature, and the vapor percentage was less than 20%. Most of the fluid inclusions occurred in clusters and in random populations (Figure 9A). Although the possibility that some of the fluid inclusions in clusters may have been secondary or pseudosecondary could not be totally ruled out, they were most likely primary [45]. Fluid inclusions in random populations were distributed evenly in a crystal without special orientation (Figure 9B), and they were also considered to be primary despite the possibility that some of them may have been secondary. Relatively isolated fluid inclusions in the random populations were considered more likely to be primary and were preferably selected for study. A total of 101 fluid inclusions, including 21 FIAs and 28 isolated fluid inclusions, were measured for microthermometry (Table 1).

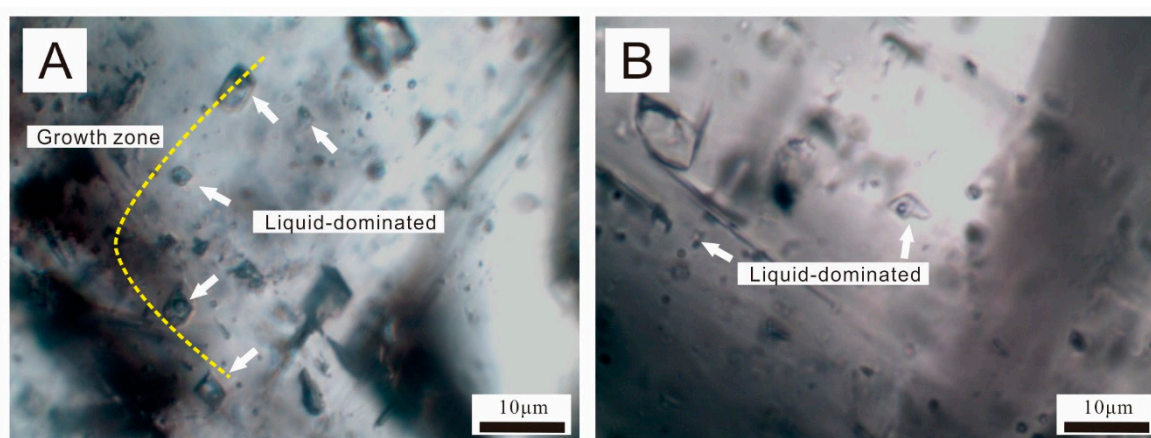


**Figure 9.** Photomicrographs showing fluid inclusion petrography. (A) Liquid-dominated fluid inclusions outlined the growth zone of Cd dolomite (Xinjigu;  $P_{2q}$ ); (B) liquid-dominated fluid inclusions in random populations were distributed evenly in a crystal without special orientation (4989.6 m; Well Hanshen1;  $P_{2q}$ ).

In Rd3 dolomite, fluid inclusions were examined in samples both from proximal and distal areas. In samples from proximal areas, fluid inclusion homogenization temperatures ranged from 182 °C to 248 °C for the FIAs (Figures 10 and 11). Ice melting temperatures ranged from −25.3 °C to −14.1 °C and salinities from 17.8 wt.% to 24.8 wt.% for the FIAs. In samples from distal areas, fluid inclusion homogenization temperature was 149 °C for one FIA and ranged from 202 °C to 203 °C for isolated fluid inclusions. The ice melting temperature for the FIA was −8.2 °C and ranged from −6.2 °C to −5.7 °C for isolated fluid inclusions, yielding salinities of 12.1 wt.% and 9.0–9.7 wt.%, respectively.

In Cd dolomite, fluid inclusions were also examined in samples both from proximal and distal areas. In samples from proximal areas, fluid inclusion homogenization temperatures ranged from 154 °C to 248 °C for FIAs and 179 °C to 255 °C for isolated fluid inclusions. Ice melting temperatures ranged from −25.3 °C to −6.9 °C for FIAs and −25.1 °C to −2.4 °C for isolated fluid inclusions, and salinities ranged from 10.5 wt.% to 24.8 wt.% for FIAs and 7.9 wt.% to 24.7 wt.% for isolated fluid inclusions. In samples from distal areas, fluid inclusion homogenization temperatures ranged from 164 °C to 194 °C for FIAs and 215 °C to 229 °C for isolated fluid inclusions, and ice melting temperature ranged from −14.2 °C to −5.5 °C for FIAs and −5.3 °C to −4.8 °C for isolated fluid inclusions. Salinities ranged from 8.7 wt.% to 17.9 wt.% for FIAs and 7.8 wt.% to 8.5 wt.% for isolated fluid inclusions.

In calcite cements, fluid inclusion homogenization temperatures ranged from 135 °C to 175 °C for isolated fluid inclusions. For isolated fluid inclusions, ice melting temperatures ranged from −15.4 °C to −9.2 °C, and salinities ranged from 13.2 wt.% to 18.9 wt.%.

**Table 1.** Fluid inclusion data of Rd3 and Cd dolomite in Middle Permian in southwest (SW) Sichuan Basin.  $T_h$ —homogenization temperature;  $T_{m-ice}$ —ice melting temperature; XJG—Xinjigu outcrop; ZC—Zhangcun outcrop; HS1—Well Hanshen1.

Sample	Host Mineral	Occurrences	V (%)	$T_h$ (°C)	$T_{m-ice}$ (°C)	Salinity (wt.%)
XJG-3-2	Cd	Isolated	20	215	−5.3	8.5
XJG-3-2	Cd	Isolated	30	229	−4.8	7.8
XJG-3-2	Cd	Isolated	30	229	−4.9	7.9
XJG-3-2	Cd	Isolated	30	220	−4.8	7.8
XJG-4-1	Rd3	Isolated	30	203	−6.2	9.7
XJG-4-1	Rd3	Isolated	20	202	−5.7	9.0
XJG-4-1	Rd3	Cluster	30	149	−8.2	12.1
XJQ-3-1	Cd	Cluster	20	164	−5.5	8.7
XJQ-3-1	Cd	Cluster	20	183	−6.0	9.4
XJQ-3-1	Cd	Cluster	20	169	−8.5	12.4
XJQ-3-1	Cd	Cluster	20	164	−8.6	12.5
XJQ-3-1	Cd	Cluster	20	184	−7.9	11.7
XJQ-3-1	Cd	Cluster	20	194	−14.2	17.9
XJQ-3-1	Cd	Cluster	20	177	−12.0	15.9
XJQ-3-1	Cd	Cluster	20	176	−6.4	9.9
XJQ-3-1	Cd	Cluster	30	173	−7.9	11.7
XJQ-3-1	Cd	Cluster	30	189	−8.6	12.5
ZC-24	Cd	Isolated	30	239	−2.4	4.1
ZC-24	Cd	Isolated	30	240	−24.3	24.4
ZC-24	Cd	Isolated	20	192	−10.6	14.6
ZC-24	Cd	Isolated	40	190	−8.5	12.4
ZC-24	Cd	Isolated	20	198	−4.9	7.9
ZC-24	Cd	Isolated	20	179	−10.9	14.9
ZC-24	Cd	Isolated	20	179	−11.2	15.2
ZC-24	Cd	Isolated	30	220	−10.5	14.5
ZC-24	Cd	Isolated	20	224	−8.6	12.5
ZC-24	Cd	Isolated	20	225	−8.8	12.7
ZC-24	Cd	Isolated	30	191	−8.4	12.3
ZC-29	Cd	Isolated	35	234	−25.1	24.7
ZC-29	Cd	Isolated	40	255	−21.6	23.5
ZC-29	Cd	Isolated	20	204	−15.6	19.0
ZC-29	Cd	Isolated	20	189	−21.3	23.4
ZC-29	Cd	Isolated	30	255	−19.2	21.8
HS1-4973.8	Cd	Cluster	30	154	−13.8	17.5
HS1-4973.8	Cd	Cluster	20	192	−10.6	14.6
HS1-4973.8	Cd	Cluster	20	221	−15.2	18.7
HS1-4988.5	Cd	Cluster	30	209	−11.3	15.3
HS1-4988.5	Cd	Cluster	30	219	−6.9	10.5
HS1-4989.6	Rd3	Cluster	20	225	−14.7	18.3
HS1-4989.6	Rd3	Cluster	20	182	−14.1	17.8
HS1-4989.6	Rd3	Cluster	20	248	−25.3	24.8
HS1-4989.6	Rd3	Cluster	20	185	−24.8	24.6
HS1-4989.6	Cd	Cluster	20	248	−25.3	24.8
HS1-4913.4	Cc	Isolated	20	157	−15.4	18.9
HS1-4913.4	Cc	Isolated	20	136	−14.8	18.4
HS1-4913.4	Cc	Isolated	20	175	−9.2	13.2
HS1-4913.4	Cc	Isolated	10	168	−10.5	14.5
HS1-4913.4	Cc	Isolated	20	173	−12.8	16.6
HS1-4913.4	Cc	Isolated	10	169	−13.5	17.3

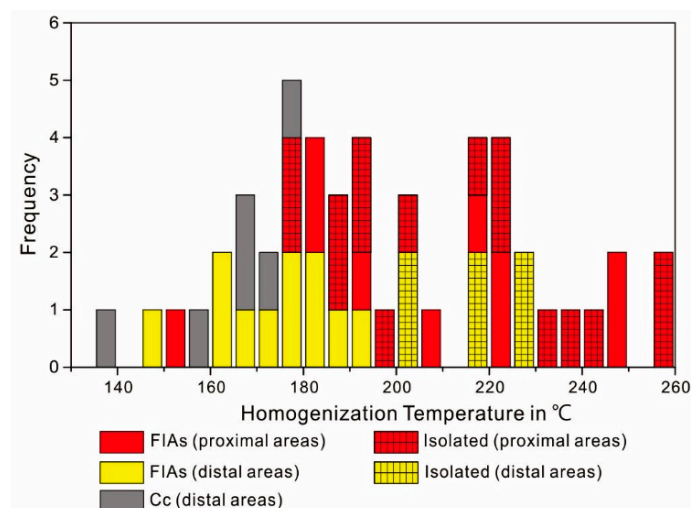


**Figure 10.** Histograms of homogenization temperatures of fluid inclusion assemblages (FIA) and isolated fluid inclusions.

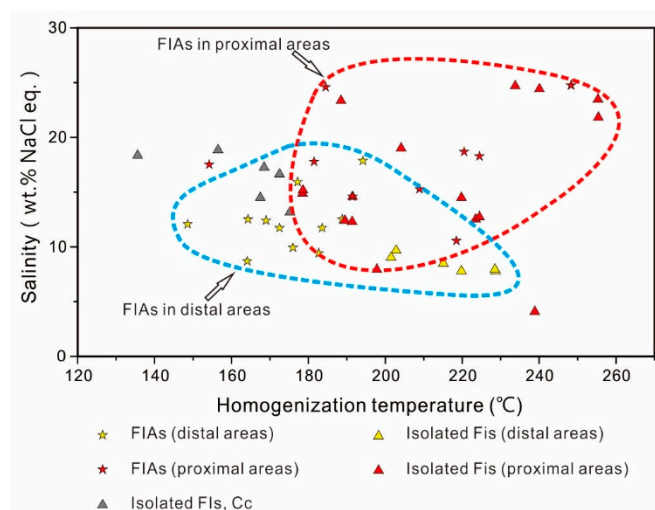


**Figure 11.** Cross-plot of salinity, calculated from final melting temperatures ( $T_m$ ) of FIAs and isolated fluid inclusions, versus homogenization temperatures ( $T_h$ ) from FIAs and isolated fluid inclusions of Rd3 and Cd dolomite.

#### 4.3. Carbon and Oxygen Isotopes

Most bioclastic limestone and Rd1 and Rd2 dolomite samples for carbon and oxygen isotope analysis were collected from distal areas, and Rd3 samples were collected from both proximal and distal areas, whereas Cd samples were only collected from proximal areas. The  $\delta^{18}\text{O}_{\text{VPDB}}$  value of bioclastic limestone was  $-6.1\text{‰}$  and the  $\delta^{13}\text{C}_{\text{VPDB}}$  value was  $3.8\text{‰}$ . Rd1 dolomite had  $\delta^{18}\text{O}_{\text{VPDB}}$  values between  $-7.4\text{‰}$  and  $-5.2\text{‰}$ , and  $\delta^{13}\text{C}_{\text{VPDB}}$  values between  $-0.4\text{‰}$  and  $4.3\text{‰}$  (Table 2; Figure 12). Rd2 dolomite yielded  $\delta^{18}\text{O}_{\text{VPDB}}$  values from  $-6.6\text{‰}$  to  $-5.5\text{‰}$  and  $\delta^{13}\text{C}_{\text{VPDB}}$  values from  $-0.0\text{‰}$  to  $4.9\text{‰}$ . Rd3 dolomite samples were collected from both distal and proximal areas. For Rd3 dolomite samples from distal areas, the  $\delta^{18}\text{O}_{\text{VPDB}}$  and  $\delta^{13}\text{C}_{\text{VPDB}}$  values spanned from  $-12.0\text{‰}$  to  $-9.1\text{‰}$  and from  $1.2\text{‰}$  to  $4.0\text{‰}$ , respectively, whereas, for Rd3 dolomite from proximal areas, the  $\delta^{18}\text{O}_{\text{VPDB}}$  and  $\delta^{13}\text{C}_{\text{VPDB}}$  values spanned from  $-12.0\text{‰}$  to  $-10.1\text{‰}$  and from  $3.4\text{‰}$  to  $4.9\text{‰}$ , respectively (Table 2; Figure 12).

**Table 2.** Stable isotope data of limestone and dolomite in Middle Permian in SW Sichuan Basin. XJG—Xinjigu outcrop; ZC—Zhangcun outcrop; HS1—Well Hanshen1.

Sample Identification				Stable Isotopes				
Well/Outcrop	Strata	Sample	Minerals	$\delta^{13}\text{C}$ (‰, VPDB)	$\delta^{18}\text{O}$ (‰, VPDB)	$\text{C}_{\text{fluid}}$ (‰, VPDB)	$\text{O}_{\text{fluid}}$ (‰, SMOW)	$^{87}\text{Sr}/^{86}\text{Sr}$
XJG	<i>P</i> <sub>2q</sub>	XJG-3	Rd1	−0.37	−5.19			
XJG	<i>P</i> <sub>2m</sub>	XJG-51	Rd1	4.23	−7.39			0.707795
XJG	<i>P</i> <sub>2m</sub>	XJG-55	Rd1	4.32	−6.76			0.707941
XJG	<i>P</i> <sub>2q</sub>	XJG-5-D	Rd1	3.44	−7.41			0.707085
XJG	<i>P</i> <sub>2q</sub>	XJG-19-D	Rd1	4.09	−6.65			0.707768
XJG	<i>P</i> <sub>2q</sub>	XJG-8	Rd2	−0.04	−5.80			0.707951
XJG	<i>P</i> <sub>2q</sub>	XJG-13	Rd2	0.31	−5.50			0.707292
XJG	<i>P</i> <sub>2q</sub>	XJG-18	Rd2	0.47	−5.73			0.707565
XJG	<i>P</i> <sub>2q</sub>	XJG-25	Rd2	2.06	−6.59			
XJG	<i>P</i> <sub>2m</sub>	XJG-66	Rd2	4.89	−5.49			
XJG	<i>P</i> <sub>2q</sub>	XJG-5	Rd2	0.07	−5.89			
XJG	<i>P</i> <sub>2q</sub>	XJG-6	Rd2	−0.18	−4.96			
XJG	<i>P</i> <sub>2q</sub>	XJG-16-1B	Rd3	4.03	−9.11	2.23	9.97	
XJG	<i>P</i> <sub>2q</sub>	XJG-8-1	Rd3	1.21	−11.89	−0.59	7.10	
XJG	<i>P</i> <sub>2q</sub>	XJG-22-1	Rd3	2.14	−11.18	0.34	7.84	
XJG	<i>P</i> <sub>2q</sub>	XJG-25-2	Rd3	2.07	−10.07	0.27	8.98	
ZC	<i>P</i> <sub>2q</sub>	ZC-13a	Rd3	4.48	−10.59			0.709103
ZC	<i>P</i> <sub>2q</sub>	ZC-17	Rd3	4.30	−11.58			
ZC	<i>P</i> <sub>2q</sub>	ZC-20	Rd3	3.75	−10.66			
ZC	<i>P</i> <sub>2q</sub>	ZC-22a	Rd3	4.01	−10.86			0.708461
ZC	<i>P</i> <sub>2q</sub>	ZC-23a	Rd3	3.69	−11.45			0.708700
HS1	<i>P</i> <sub>2q</sub>	HS1-4965.5	Rd3	3.69	−11.41	1.29	10.21	0.708235
HS1	<i>P</i> <sub>2q</sub>	HS1-4966	Rd3	3.68	−11.52	3.05	9.55	0.708646
HS1	<i>P</i> <sub>2q</sub>	HS1-4971.6	Rd3	3.38	−11.76	3.06	9.48	0.708417
HS1	<i>P</i> <sub>2q</sub>	HS1-4973.8	Rd3	3.48	−10.94	2.89	9.50	0.708193
HS1	<i>P</i> <sub>2q</sub>	HS1-4977.9	Rd3	3.66	−12.01	2.58	9.14	0.708362
HS1	<i>P</i> <sub>2q</sub>	HS1-4982.6	Rd3	3.89	−11.53	4.12	10.85	0.708258
HS1	<i>P</i> <sub>2q</sub>	HS1-4989.6	Rd3	3.68	−11.46	2.88	9.45	0.708894
HS1	<i>P</i> <sub>2q</sub>	HS1-4997.2	Rd3	4.92	−10.10	2.88	9.39	0.708787
ZC	<i>P</i> <sub>2q</sub>	ZC-13b	Cd	2.09	−10.72	2.86	8.88	0.719821
ZC	<i>P</i> <sub>2q</sub>	ZC-22b	Cd	3.85	−11.36	3.09	9.37	0.710178
ZC	<i>P</i> <sub>2q</sub>	ZC-23b	Cd	3.86	−11.43	2.51	8.57	0.709582
HS1	<i>P</i> <sub>2q</sub>	HS1-4967.8	Cd	3.77	−12.00	2.97	8.89	0.708372
HS1	<i>P</i> <sub>2q</sub>	HS1-4971.3	Cd	3.31	−12.31	2.68	9.98	0.708810
ZC	<i>P</i> <sub>2q</sub>	ZC-27	CC	3.28	−8.23			
XJG	<i>P</i> <sub>2q</sub>	XJG-16	Qz					0.707292
XJG	<i>P</i> <sub>2q</sub>	XJG-27	lime	3.81	−6.10			
XJG	<i>P</i> <sub>2q</sub>	XJG-22-D	lime					0.707102

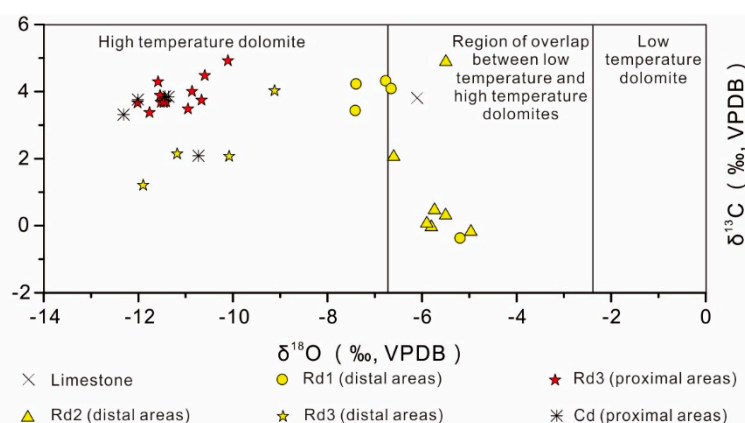


**Figure 12.** Cross-plot of  $\delta^{13}\text{C}$  and  $\delta^{18}\text{O}$  values for limestone, replacive dolomites (Rd1–Rd3), and cement dolomite (Cd). Typical ranges of isotopic values for dolomite formed in low temperatures and high temperatures [46].

The  $\delta^{18}\text{O}_{\text{VSMOW}}$  and  $\delta^{13}\text{C}_{\text{VPDB}}$  values of the parent fluids of Rd3 and Cd dolomite ( $\delta^{13}\text{C}_{\text{fluid}}$  and  $\delta^{18}\text{O}_{\text{fluid}}$ ) were calculated from the  $\delta^{18}\text{O}$  and  $\delta^{13}\text{C}$  values of the carbonate minerals, and the average temperatures were based on homogenization temperatures of the FIAs (Table 2; Figure 13). The  $\delta^{13}\text{C}_{\text{fluid-VPDB}}$  and  $\delta^{18}\text{O}_{\text{fluid-VSMOW}}$  values of Rd3 dolomite from distal areas ranged from  $-0.59\text{‰}$  to  $2.23\text{‰}$  and  $7.1\text{‰}$  to  $9.97\text{‰}$  respectively, and the  $\delta^{13}\text{C}_{\text{fluid-VPDB}}$  and  $\delta^{18}\text{O}_{\text{fluid-VSMOW}}$  values of Rd3 and Cd dolomite from proximal areas ranged from  $1.29\text{‰}$  to  $4.12\text{‰}$  and  $8.88\text{‰}$  to  $10.85\text{‰}$ , respectively (Table 2; Figure 13).

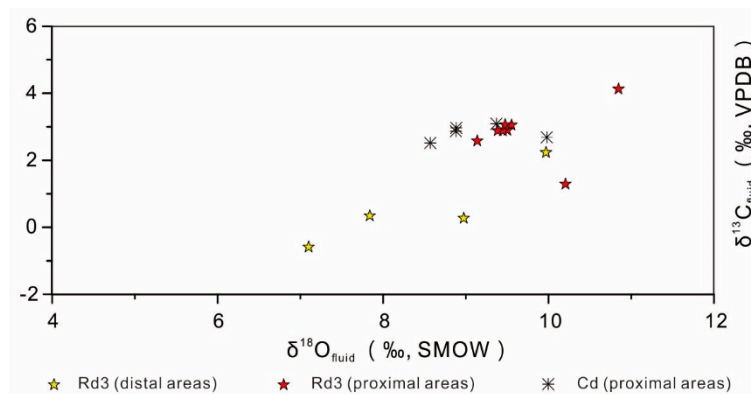


**Figure 13.** Cross-plot of  $\delta^{13}\text{C}_{\text{fluid}}$  and  $\delta^{18}\text{O}_{\text{fluid}}$  values of Rd3 and Cd dolomites, calculated from the  $\delta^{18}\text{O}$  and  $\delta^{13}\text{C}$  values of the carbonate minerals and the average temperatures based on homogenization temperatures of FIAs [38].

#### 4.4. Strontium Isotopes

The  $^{87}\text{Sr}/^{86}\text{Sr}$  ratios for the Rd1 dolomite were between 0.707085 and 0.707795, near the approximated range for Permian seawater (0.70662–0.70774) [47] (Table 2; Figure 14). The  $^{87}\text{Sr}/^{86}\text{Sr}$  ratios ranged from 0.707292 to 0.707951 for Rd2, 0.708193 to 0.709103 for Rd3, and 0.708372 to 0.719821 for Cd (Table 2; Figure 14).

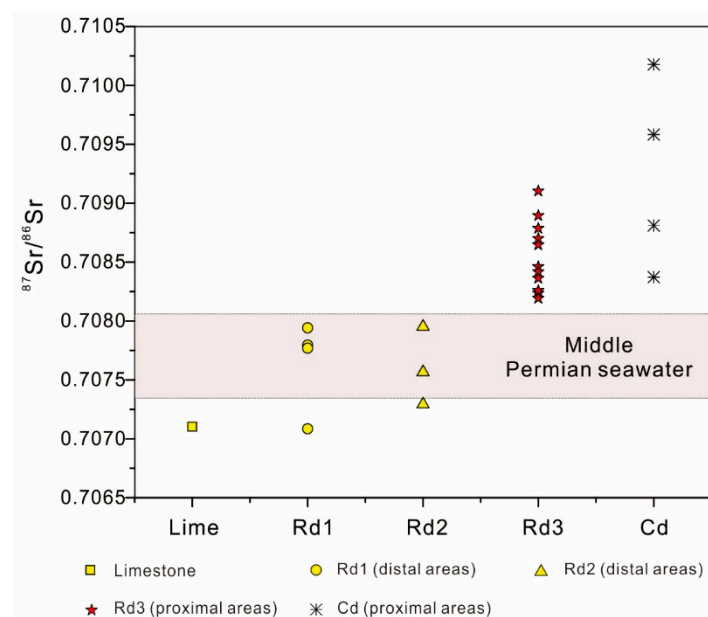


**Figure 14.**  $^{87}\text{Sr}/^{86}\text{Sr}$  ratios of limestone, replacive dolomites (Rd1–Rd3), and cement dolomite (Cd). The shaded area represents estimated  $^{87}\text{Sr}/^{86}\text{Sr}$  ratios of Middle Permian seawater (0.7074–0.7081) [47].

#### 4.5. Rare Earth Elements

The REE data were normalized to the post-Archean Australian shale (PAAS) [35] (Table 3). The limestone and Rd1 dolomite were characterized by flat REE patterns, slight light REE (LREE) enrichment (average  $Nd_{SN}/Yb_{SN} = 1.11$ ,  $n = 6$ ), and slight positive Eu anomalies (Table 3, Figures 15A, 16 and 17). Rd2 dolomite showed similar REE patterns to limestone Rd1, with slight LREE enrichment (average  $Nd_{SN}/Yb_{SN} = 1.12$ ,  $n = 5$ ), slight negative Ce anomalies, and variable Eu anomalies (Table 3, Figures 15B, 16 and 17). Rd3 dolomite from both proximal and distal areas was characterized by prominent positive Eu anomalies (average  $Eu/Eu^* = 1.53$ ,  $n = 11$ ) and heavy rare earth elements (HREE) enrichment (average  $Nd_{SN}/Yb_{SN} = 0.72$ ,  $n = 11$ ) (Table 3, Figures 15C, 16 and 17). The Cd dolomite samples had similar REE patterns to Rd3 dolomite, including significant positive Eu anomalies (average  $Eu/Eu^* = 1.23$ ,  $n = 4$ ) and HREE enrichment (average  $Nd_{SN}/Yb_{SN} = 0.81$ ,  $n = 4$ ) (Table 3, Figures 15D, 16 and 17).

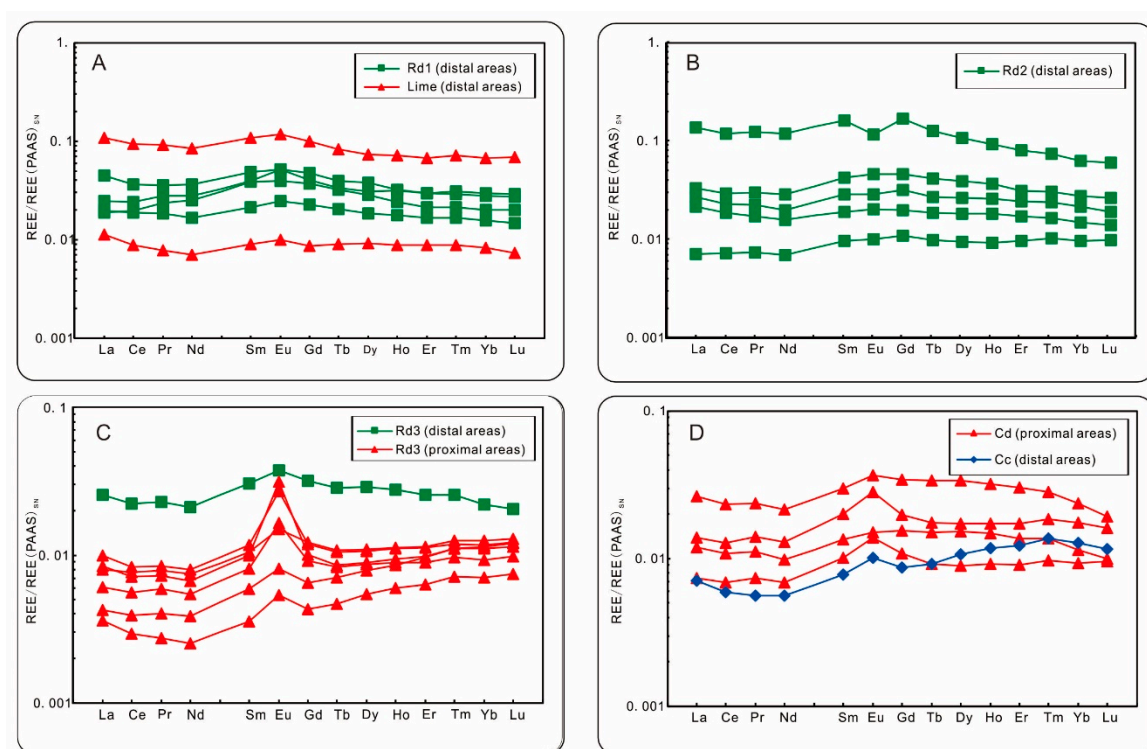


**Figure 15.** Post-Archean average shale (PAAS)-normalized rare earth element (REE) patterns of limestone and dolomites. The PAAS data were obtained from McLennan (1989) [35].

**Table 3.** Rare earth element data of limestone and dolomite in Middle Permian in SW Sichuan Basin. XJG—Xinjigu outcrop; ZC—Zhangcun outcrop; HS1—Well Hanshen1.

Sample ID	Minerals	Rare Earth Elements (REEs)																	
		La	Ce	Pr	Nd	Sm	Eu	Gd	Tb	Dy	Ho	Er	Tm	Yb	Lu	ΣREE	Nd/Yb	δEu	δCe
XJG-51	Rd1	0.7584	1.5150	0.1648	0.5698	0.1186	0.0265	0.1051	0.0159	0.0874	0.0176	0.0471	0.0067	0.0440	0.0064	3.4836	1.0777	1.1151	0.9882
XJG-74	Rd1	0.9433	1.9102	0.2446	0.9377	0.2202	0.0554	0.1897	0.0259	0.1454	0.0310	0.0851	0.0125	0.0838	0.0126	4.8975	0.9309	1.2760	0.9161
XJG-5-D	Rd1	1.7024	2.9171	0.3164	1.2302	0.2701	0.0558	0.2238	0.0309	0.1770	0.0320	0.0850	0.0118	0.0781	0.0118	7.1423	1.3104	1.0684	0.9116
XJG-19-D	Rd1	0.7217	1.5743	0.2110	0.8456	0.2131	0.0431	0.1745	0.0250	0.1336	0.0238	0.0604	0.0087	0.0561	0.0086	4.0996	1.2539	1.0525	0.9246
XJG-27	lime	0.4337	0.6951	0.0688	0.2388	0.0496	0.0107	0.0400	0.0070	0.0426	0.0088	0.0250	0.0036	0.0234	0.0032	1.6502	0.8483	1.1302	0.9124
XJG-45	lime	4.1007	7.4666	0.8072	2.8534	0.5947	0.1263	0.4641	0.0635	0.3424	0.0716	0.1907	0.0290	0.1898	0.0298	17.3299	1.2509	1.1311	0.9438
XJG-13	Rd2	0.8482	1.5137	0.1551	0.5533	0.1084	0.0222	0.0951	0.0148	0.0874	0.0184	0.0500	0.0068	0.0425	0.0062	3.5222	1.0830	1.0276	0.9563
XJG-18	Rd2	1.0565	1.8579	0.2004	0.6842	0.1613	0.0316	0.1509	0.0213	0.1260	0.0260	0.0711	0.0098	0.0618	0.0085	4.4673	0.9215	0.9530	0.9271
XJG-25	Rd2	5.3638	9.5941	1.1239	4.0961	0.9209	0.1278	0.8066	0.1000	0.5068	0.0932	0.2351	0.0307	0.1801	0.0264	23.2054	1.8922	0.6983	0.9005
XJG-66	Rd2	0.2755	0.5841	0.0660	0.2398	0.0548	0.0112	0.0517	0.0078	0.0452	0.0094	0.0280	0.0042	0.0278	0.0044	1.4098	0.7181	0.9868	0.9990
XJG-8	Rd2	1.2915	2.3717	0.2721	0.9877	0.2419	0.0506	0.2206	0.0327	0.1850	0.0370	0.0901	0.0125	0.0799	0.0118	5.8851	1.0285	1.0313	0.9222
XJG-5	Rd3	0.9832	1.7842	0.2012	0.7176	0.1698	0.0403	0.1480	0.0222	0.1354	0.0276	0.0734	0.0103	0.0621	0.0089	4.3841	0.9618	1.1969	0.9238
ZC-13a	Rd3	0.3903	0.7501	0.0939	0.3308	0.0686	0.0170	0.0661	0.0110	0.0677	0.0139	0.0400	0.0062	0.0423	0.0072	1.9049	0.6507	1.1840	0.9040
ZC-17	Rd3	1.4960	2.9324	0.3146	1.0653	0.2219	0.0445	0.1611	0.0232	0.1347	0.0260	0.0720	0.0106	0.0699	0.0107	6.5830	1.2668	1.1056	0.9852
ZC-22a	Rd3	0.4115	0.8315	0.0951	0.3443	0.0748	0.0148	0.0615	0.0096	0.0576	0.0111	0.0293	0.0042	0.0279	0.0044	1.9776	1.0253	1.0253	0.9697
ZC-23a	Rd3	0.7482	1.6726	0.1958	0.6801	0.1421	0.0274	0.1280	0.0197	0.1129	0.0223	0.0601	0.0095	0.0671	0.0093	3.8951	0.8426	0.9554	1.0063
HS1-4965.5	Rd3	0.3820	0.6587	0.0741	0.2711	0.0650	0.0292	0.0550	0.0081	0.0498	0.0110	0.0321	0.0048	0.0328	0.0053	1.6791	0.6870	2.2961	0.9000
HS1-4997.2	Rd3	0.3202	0.5684	0.0638	0.2272	0.0550	0.0338	0.0466	0.0066	0.0419	0.0093	0.0279	0.0045	0.0312	0.0049	1.4413	0.6061	3.1444	0.9150
HS-4989.6	Rd3	0.1621	0.3103	0.0355	0.1310	0.0328	0.0087	0.0302	0.0055	0.0370	0.0085	0.0274	0.0045	0.0320	0.0052	0.8310	0.3401	1.3072	0.9434
HS-4966	Rd3	0.2304	0.4456	0.0521	0.1843	0.0451	0.0177	0.0425	0.0064	0.0404	0.0088	0.0255	0.0039	0.0262	0.0042	1.1331	0.5861	1.9028	0.9381
HS-4977.9	Rd3	0.3054	0.6117	0.0694	0.2516	0.0581	0.0162	0.0567	0.0084	0.0513	0.0111	0.0325	0.0050	0.0355	0.0055	1.5185	0.5897	1.3243	0.9689
HS-4982.6	Rd3	0.1380	0.2348	0.0242	0.0859	0.0197	0.0058	0.0200	0.0036	0.0253	0.0059	0.0181	0.0029	0.0200	0.0032	0.6075	0.3582	1.3688	0.9289
ZC-13b	Cd	0.5319	1.0198	0.1247	0.4390	0.1108	0.0307	0.0926	0.0136	0.0808	0.0170	0.0491	0.0075	0.0490	0.0070	2.5734	0.7455	1.4250	0.9135
ZC-22b	Cd	0.4564	0.8604	0.0980	0.3315	0.0751	0.0163	0.0720	0.0116	0.0709	0.0148	0.0391	0.0055	0.0322	0.0043	2.0879	0.8573	1.0399	0.9382
ZC-23b	Cd	1.0032	1.8517	0.2099	0.7320	0.1655	0.0394	0.1590	0.0261	0.1578	0.0316	0.0859	0.0115	0.0665	0.0084	4.5484	0.9150	1.1407	0.9299
HS1-4971.3	Cd	0.2811	0.5469	0.0649	0.2341	0.0561	0.0149	0.0508	0.0071	0.0416	0.0091	0.0258	0.0039	0.0263	0.0042	1.3667	0.7415	1.3171	0.9345
XJG-70	Cc	0.2711	0.4734	0.0498	0.1912	0.0433	0.0108	0.0407	0.0071	0.0498	0.0116	0.0350	0.0055	0.0360	0.0050	1.2302	0.4423	1.2158	0.9337

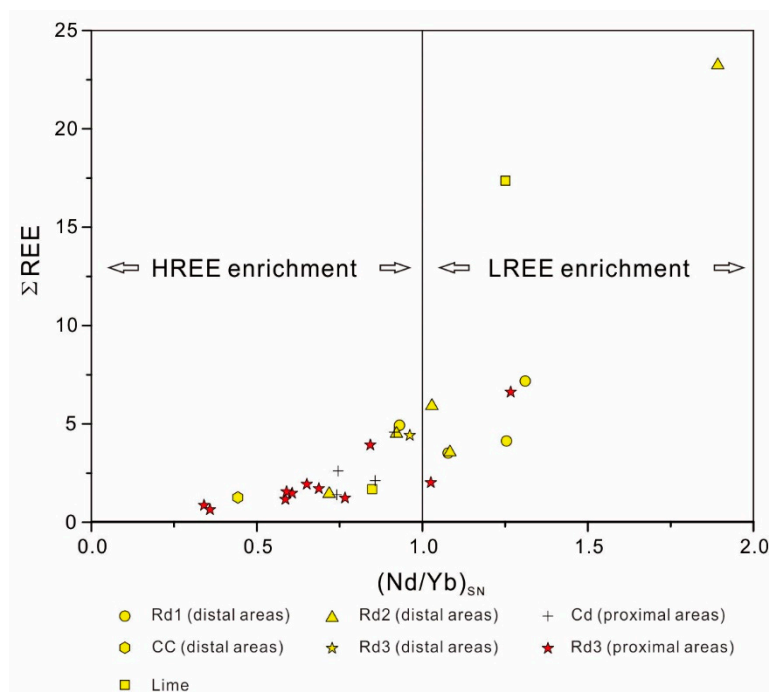


**Figure 16.** Cross-plot of total REE and  $\text{Nd}_{\text{SN}}/\text{Yb}_{\text{SN}}$  of limestone and dolomite shows light REE (LREE) or heavy REE (HREE) enrichment [48]. Field of LREE enrichment:  $\text{Nd}_{\text{SN}}/\text{Yb}_{\text{SN}} > 1$ ; field of HREE enrichment:  $\text{Nd}_{\text{SN}}/\text{Yb}_{\text{SN}} < 1$ .

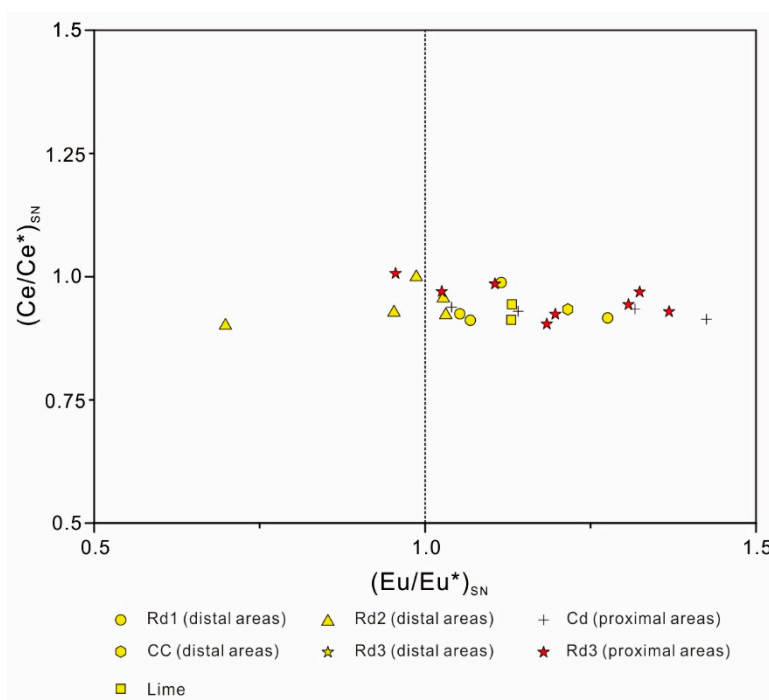


**Figure 17.** Cross-plot of  $\text{Eu}/\text{Eu}^*$  and  $\text{Ce}/\text{Ce}^*$  of limestone and dolomite shows Ce anomalies and Eu anomalies.

### 5. Discussion

The dolomite reservoirs in the Middle Permian strata in the southwestern Sichuan Basin contain multiple phases of dolomite, and it was proposed that some of them are of hydrothermal nature [18–20]. However, it is not clear which phases of dolomite may be hydrothermal and on what basis they are considered as hydrothermal dolomites. Furthermore, it remains poorly understood how the

dolomitization processes in areas proximal and distal to fault zones may be related to each other, and what controlled the distribution of different phases of dolomite.

Most of the Rd1 dolomites had micritic to fine crystals with planar-s to nonplanar-a textures (Figure 4), which are likely linked to penecontemporaneous to shallow burial dolomitization at low temperatures [12,49–51]. The preservation of sedimentary fabrics of precursor limestones (bioclasts and sand-clast) (Figure 4B,C) was most likely caused by the selective dolomitization of the matrix during a shallow burial process: the matrix had much smaller grain sizes and higher permeability with a larger reactive surface area than the larger biochems/peloids, which made it more susceptible to dolomitization and dissolution [52]. The average  $\delta^{13}\text{C}_{\text{VPDB}}$  value (3.14‰,  $n = 5$ ) of Rd1 dolomite was very close to the average Middle Permian marine carbonates (2.86‰,  $n = 78$ ) in the Upper Yangtze area [53]. The  $\delta^{18}\text{O}_{\text{VPDB}}$  values (−7.41‰ to −5.19‰) were comparable to those of dolomites developed in equilibrium with Middle Permian seawater [54], and were significantly lower than those of Permian extremely evaporative dolomites (+0.2‰ to +7.4‰) [55]. The C and O isotope data suggest that Rd1 formed from reflux of penecontemporaneous seawater in shallow burial conditions [12,52,56], with the dolomitizing fluids being mesosaline or penesaline rather than greatly evaporated brines [57]. During the Middle Permian, the southwestern Sichuan Basin was situated within the platform interior (Figure 1), where the circulation of seawater with the open marine was more or less restricted and could have enhanced evaporation [12,13,58]. During the shallow burial stage in the penecontemporaneous period, evaporated seawater with increased Mg/Ca ratio flowed down the platform or through the platform sediments to the sea due to increased density, resulting in the dolomitization of sediments infiltrated with high Mg/Ca ratio seawater [59,60]. This seepage/reflux dolomitization may have caused the formation of Rd1 dolomite. In low-energy depositional environments (e.g., lagoons), Rd1 dolomite preserved the horizontal stratification of the original limestone (Figure 4A) and preserved the original grains in high-energy depositional zones (e.g., grain shoals) both in proximal and distal areas (Figure 4B). This hypothesis is further supported by the  $^{87}\text{Sr}/^{86}\text{Sr}$  ratios (0.707085 to 0.707795), which greatly overlap with the Permian seawater (0.70662 to 0.70774) [47].

The planar euhedral to subhedral crystals of Rd2 dolomite (Figure 5A–C) suggest that the formation temperature was lower than the critical roughening temperature (CRT, 50–60 °C), and were formed in a shallow burial environment [49,50]. The  $\delta^{18}\text{O}_{\text{VPDB}}$  values (−6.6‰ to −5.5‰) of Rd2 dolomite were broadly consistent with these kinds of thermal conditions (Figure 12). Meanwhile, the similarity in  $^{87}\text{Sr}/^{86}\text{Sr}$  ratios (Figure 13) and REE patterns (Table 3, Figures 15B, 16 and 17) between Rd1 and Rd2 supports the notion that Rd2 dolomite was precipitated from connate penecontemporaneous seawater preserved in the formations [61], although at a slightly higher temperature than for Rd1. The increased crystal size of Rd2 relative to Rd1 may have been due to the enhanced release of Mg ions caused by the compaction of overlying sediments and the resultant pressure dissolution, which may have promoted dolomite crystallization [13,62,63], as recorded by the clear rims overgrowing the cloudy cores (Figure 5C,D).

Compared with Rd1 and Rd2 dolomite, Rd3 and Cd dolomite were significantly coarser and showed more curved crystals (Figures 6 and 7), indicating rapid growth at relatively high temperatures [12,13,49,50,61]. Cd dolomite crystals that displayed an opaque to translucent white color had abundant inclusions, which implies rapid crystal growth [13,52]. Rd3 dolomite and Cd dolomite were likely formed from fluids with similar compositions because of their close spatial association, the transitional contact between them along the margin of vugs and fractures (Figure 7B,C), and their similar C–O–Sr isotopes and REE patterns. The homogenization temperatures of fluid inclusions (Figure 10) from Rd3 and Cd clearly indicate that they were formed at much higher temperatures than Rd1 and Rd2, which is also supported by the oxygen isotope data (Figure 12). Cd dolomite precipitated directly from the dolomitization fluids and exhibited bright mottled luminescence in CL, which was different from the Rd3 dolomite.

The salinities of fluid inclusions in Rd3 and Cd dolomite calculated from the final melting temperature ( $T_m$ ) ranged from 10.6 wt.% to 24.8 wt.% NaCl equivalent (average 18.7%), which was up to more than five times the salinity of modern seawater, indicating that the dolomitizing fluids were basinal brines [6,13,64,65]. The increased  $^{87}\text{Sr}/^{86}\text{Sr}$  ratios may have been caused by the interaction between the dolomitizing fluids and feldspar-rich siliciclastic rocks during the upward migration from the lower part of the basin, as well as basement to the dolomitization strata [6]. The prominent positive Eu anomalies of Rd3 and Cd dolomite (Figure 15C,D) suggest that the dolomitizing fluids were more reducing than those associated with Rd1 and Rd2, thus favoring the development of  $\text{Eu}^{2+}$  which can favorably substitute Ca in the dolomite [13,66–68].

The paragenetic sequence (Figure 18) was established based on the cross-cutting relationships observed in the field, hand samples, and thin sections, as illustrated in Figure 9. Rd1 dolomite was interpreted to have formed in penecontemporaneous period, whereas Rd2 dolomite formed in a shallow burial depth, as Rd2 appeared to recrystallize from Rd1 (Figure 4E). Rd2 was further crystallized to Rd3, which was transitional to Cd (Figure 7A). Cd dolomite occurred as cement lining the wall of the hydrofractures, suggesting that Cd postdated hydraulic which may have been caused by elevated pore fluid pressure. Quartz occurred as cement in the intercrystalline pores of Rd3 dolomite (Figure 6B), and may have been formed at the same time or slightly later than Cd. Calcite cements in microfractures cross-cut the quartz cement and Rd3 dolomite, and were in turn cross-cut by stylolites and associated bitumen (Figure 7C), which represent the latest diagenetic event recorded (Figure 18).

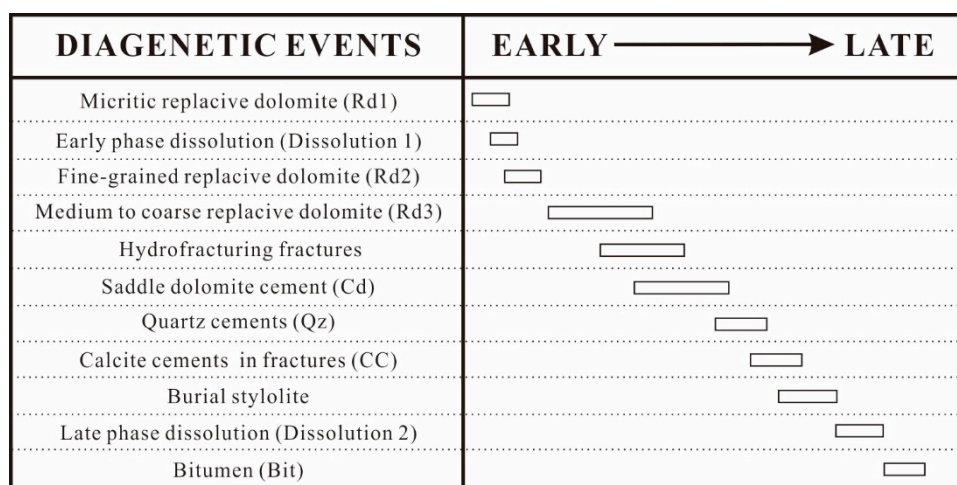


**Figure 18.** The diagenetic sequence of Middle Permian in SW Sichuan Basin.

Although the petrographic and geochemical data all support the proposal that Rd3 and Cd were formed at elevated temperatures, it does not mean that these dolomites were of a hydrothermal nature; according to Machel (2004) [48], a dolomite is qualified as hydrothermal dolomite only if the dolomitizing fluids were hotter than the surrounding rocks during the dolomitization. Thus, it is important to estimate the burial depth and temperature of the Middle Permian carbonates in southwestern Sichuan Basin during the formation of Rd3 and Cd. According to the burial curve of the Hanshen1 Well (Figure 3), the Permian strata were gradually buried to a maximum depth of about 6 km in the middle of Cenozoic, and then started to uplift. The observation that stylolites cross-cut Rd3 and Cd dolomite (Figure 6A,B) puts a major constraint on the timing of Rd3 and Cd dolomite; it suggests that these dolomite phases were probably formed before being buried to a depth of 600–1500 m, as most stylolites were formed at such depths [61,69–71]. Thus, the formation of Rd3 and Cd may have taken place during late Permian based on the burial curve (Figure 3). At a depth of 600–1500 m, the burial temperature would be less than 85 °C if a thermal gradient of 40 °C/km and a surface temperature of 25 °C are assumed. Thus, the temperatures of the dolomitizing fluids of Rd3 and Cd, as reflected by fluid inclusion homogenization temperatures from 136 °C to 255 °C (Figure 10),

were much higher than the estimated normal burial temperature (85 °C). This may be explained by two mechanisms: (1) abnormally high geothermal gradients over a large area (i.e., both the fluids and the ambient rocks were heated to elevated temperatures), and (2) hydrothermal fluids advecting into a low-temperature ambience (i.e., the fluids were hotter than the surrounding rocks) [6,61,72]. The fact that Rd3 and Cd were locally developed and Rd1 and Rd2 were well preserved in areas without or with limited Rd3 and Cd supports the second scenario, i.e., Rd3 and Cd were formed from hydrothermal fluids.

Based on regional tectonic settings, the hydrothermal dolomitization event may be linked with the Emeishan Large Igneous Province (ELIP), which covers a vast area in southwestern China, including part of the Sichuan Basin. Although there is dispute over the eruption age, duration, uplifting degree, and axial position of the ELIP [73,74], it is generally believed that the Upper Yangtze and its surrounding areas experienced elevated heat flow in relation to the ELIP, starting at ca. 290 Ma, reaching the peak value at ca. 259 Ma, and reducing to normal values at ca. 230 Ma (Figure 3) [32,75], which overlaps with the depositional period of the Middle Permian strata from ca. 267 Ma to ca. 257 Ma [75]. It was estimated that the paleo-geothermal gradient in the Sichuan Basin was up to 65 °C /km during the eruption of Emeishan Basalt [76]. However, even at such a thermal gradient, the burial temperature at a depth of 1500 m would still be much lower than the dolomitizing fluids of Rd3 and Cd, again attesting to the hydrothermal nature of the dolomitization.

The hydrothermal dolomitizing fluids may have been derived from the deeper part of the basin, and were channeled along basement-rooted faults to the Middle Permian strata, where the carbonates were dolomitized (Rd1 and Rd2). Deep-seated processes in association with the ELIP may have resulted in frequent faulting and hydrofracturing, favoring the reworking of preexisting dolomite and precipitation of dolomite cements in fractures and void space. In areas proximal to the faults, Rd1 and Rd2 were extensively modified to Rd3, and Cd was intensively developed, creating zebra fabrics in the rocks. The hydrothermal dolomitizing fluids may have continued to migrate laterally along the strata due to increased porosity and permeability associated with the Rd1 and Rd2 dolomitization. With increasing distance from the feeder faults, the temperature of the dolomitizing fluids decreased, and less and less Rd1 and Rd2 were recrystallized to Rd3. As a result, in distal areas far away from the faults, only a small amount of Rd3 and a minor amount of Cd were developed. The decrease in fluid temperature from the proximal to distal areas was well recorded by fluid inclusion homogenization temperatures (Figures 11 and 12). The cause of the decrease of salinities might be the incorporation of other fluids of relatively low salinities. The salinity of Permian seawater was 2.3% [77]; thus, the decreased fluid salinities in the distal areas (Figure 11) may be the result of mixing of the hydrothermal fluids with residual seawater in the strata.

Therefore, the dolomites in the Middle Permian carbonates in the southwestern Sichuan Basin were combined results from early diagenetic dolomitization (Rd1 and Rd2) and hydrothermal dolomitization (Rd3 and Cd). The distribution of the dolomites were, thus, controlled both by early diagenetic dolomitization (for Rd1 and Rd2) and structures (for Rd3 and Cd). Based on inference that Rd3 and Cd were developed as early as Permian time, as discussed above, and the observation that the vugs and fractures linked to Rd3 and Cd were filled with bitumen (Figure 6B,C and Figure 8F), all the dolomitization events probably took place prior to hydrocarbon charge and, thus, played an important role in shaping the reservoir quality and distribution. According to a previous study [78], a large hydrocarbon generation event occurred in Middle to Late Triassic, and the reservoirs created from the multiple dolomitization events in the Middle Permian carbonates could be used for hydrocarbon charging (Figure 19).

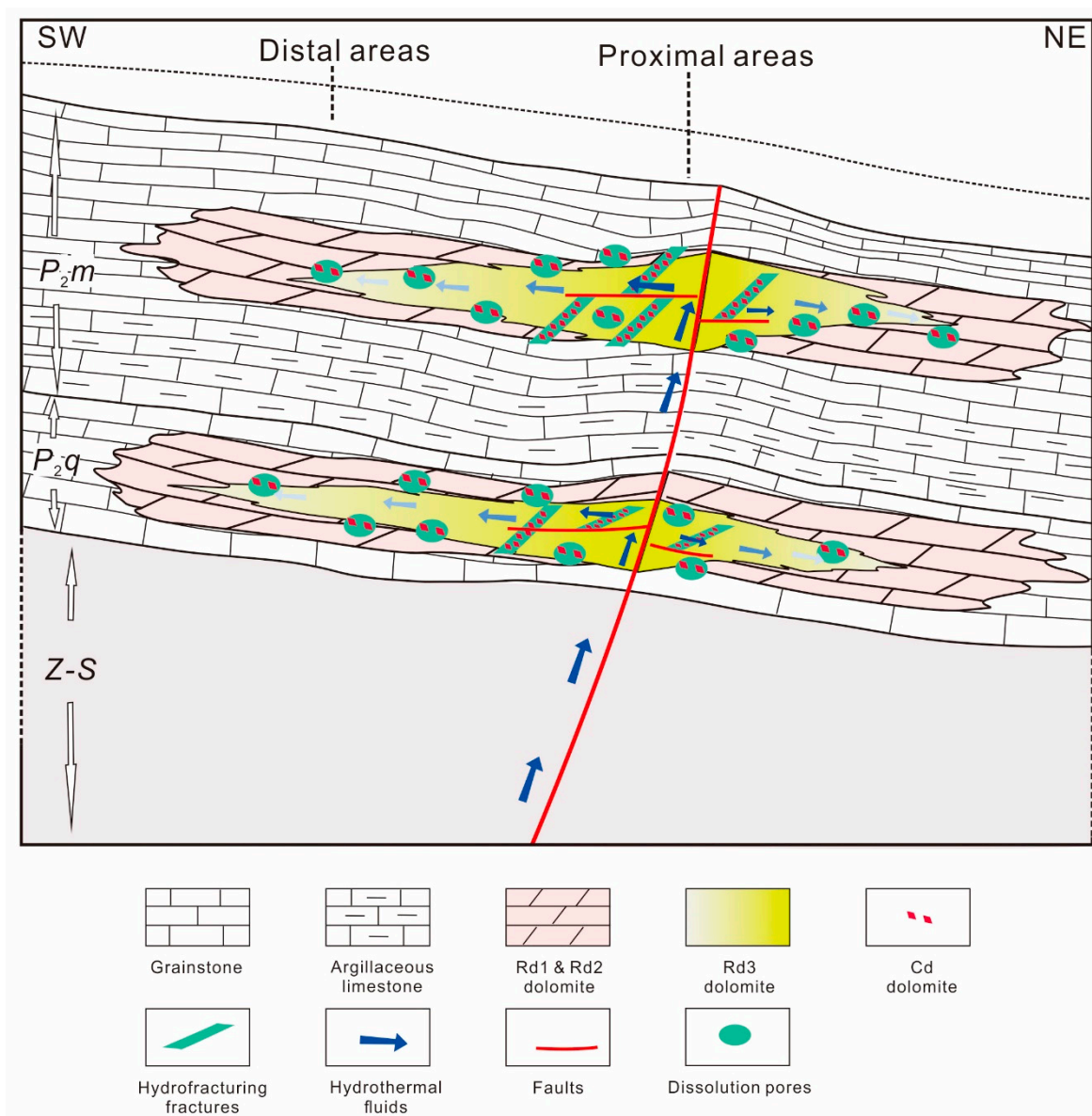


**Figure 19.** A model of multiple dolomitization events in the Middle Permian carbonates.

## 6. Conclusions

A detailed petrographic study of Middle Permian carbonate reservoir rocks in the southwestern Sichuan Basin revealed four types of dolomites, namely replacive dolomites (Rd1, Rd2, and Rd3) and dolomite cements (Cd). In areas proximal to faults, Rd3 dolomite was dominant among replacive dolomites and Cd was extensively developed in fractures and dissolution pores, whereas, in distal areas far away from faults, Rd1 and Rd2 were dominant replacive dolomites, and only a small amount of Rd3 was formed from recrystallization of Rd1 and Rd2, and minor Cd dolomite occurred in some dissolution pores.

Petrographic and geochemistry studies indicated that Rd1 dolomite was formed by the seepage/reflux dolomitization in the penecontemporaneous stage from evaporated seawater, and Rd2 dolomite was formed from connate seawater during the shallow burial stage. The Rd3 and Cd dolomite were the products of hydrothermal dolomitization from basinal brines channeling along faults and derived from deeper parts of the basin, with the elevated temperature being related to the Emeishan basalt in the Emeishan Large Igneous Province.

The dolomite reservoirs in the Middle Permian carbonates in the southwestern Sichuan Basin were dually controlled by early burial diagenesis and cross-formational faults (for hydrothermal dolomites). As the reservoirs were developed before a major hydrocarbon generation event in Middle to Late Triassic, the controlling factors of the reservoirs as revealed in this study are important for petroleum exploration.

**Author Contributions:** Data curation, J.L. and Y.W.; formal analysis, X.Z.; investigation, J.L. and Y.W.; resources, B.L.; supervision, Y.M., G.C., B.L., and X.Z.; writing—original draft, H.Z.; writing—review and editing, H.Z., G.C., H.Q., and Y.S.

**Funding:** This research was funded by the National Natural Science Foundation of China, grant number 41672123 and 41572117, and the National Science and Technology Major Project of China, grant number 2017ZX05005-003-005.

**Acknowledgments:** The paper was written when the first author was a visiting PhD student at the Department of Geology, University of Regina, supported by the China Scholarship Council (CSC).

**Conflicts of Interest:** The authors declare no conflicts of interest.

## References

1. Feng, M.; Wu, P.; Qiang, Z.; Liu, X.; Duan, Y.; Xia, M. Hydrothermal dolomite reservoir in the Precambrian Dengying Formation of central Sichuan Basin, southwestern China. *Mar. Pet. Geol.* **2017**, *82*, 206–219. [[CrossRef](#)]
2. Mahboubi, A.; Nowrouzi, Z.; Al-Aasm, I.S.; Moussavi-Harami, R.; Mahmudy-Gharaei, M.H. Dolomitization of the Silurian Niur Formation, Tabas block, east central Iran: Fluid flow and dolomite evolution. *Mar. Pet. Geol.* **2016**, *77*, 791–805. [[CrossRef](#)]
3. Wendte, J.; Chi, G.; Al-Aasm, I.; Sargent, D. Fault/fracture controlled hydrothermal dolomitization and associated diagenesis of the Upper Devonian Jean Marie Member (Redknife Formation) in the July Lake area of northeastern British Columbia. *Bull. Can. Pet. Geol.* **2009**, *57*, 275–322. [[CrossRef](#)]
4. Machel, H.-G.; Mountjoy, E.W. Chemistry and environments of dolomitization—A reappraisal. *Earth-Sci. Rev.* **1986**, *23*, 175–222. [[CrossRef](#)]
5. Chen, D.; Qing, H.; Yang, C. Multistage hydrothermal dolomites in the Middle Devonian (Givetian) carbonates from the Guilin area, South China. *Sedimentology* **2004**, *51*, 1029–1051. [[CrossRef](#)]
6. Davies, G.R.; Smith, L.B., Jr. Structurally controlled hydrothermal dolomite reservoir facies: An overview. *Aapg Bull.* **2006**, *90*, 1641–1690. [[CrossRef](#)]
7. Smith, L.B., Jr. Origin and reservoir characteristics of Upper Ordovician Trenton–Black River hydrothermal dolomite reservoirs in New York. *AAPG Bull.* **2006**, *90*, 1691–1718. [[CrossRef](#)]
8. Lavoie, D.; Chi, G. Hydrothermal dolomitization in the Lower Silurian La Vieille Formation in northern New Brunswick: Geological context and significance for hydrocarbon exploration. *Bull. Can. Pet. Geol.* **2006**, *54*, 380–395. [[CrossRef](#)]
9. Smith, L.B.; Davies, G.R. Structurally controlled hydrothermal alteration of carbonate reservoirs: Introduction. *AAPG Bull.* **2006**, *90*, 1635–1640. [[CrossRef](#)]
10. Friedman, G.M. Structurally controlled hydrothermal dolomite reservoir facies: An overview: Discussion. *AAPG Bull.* **2007**, *91*, 1339–1341. [[CrossRef](#)]
11. Lavoie, D.; Chi, G.; Urbatsch, M.; Davis, W. Massive dolomitization of a pinnacle reef in the Lower Devonian West Point Formation (Gaspé Peninsula, Quebec): An extreme case of hydrothermal dolomitization through fault-focused circulation of magmatic fluids. *AAPG Bull.* **2010**, *94*, 513–531. [[CrossRef](#)]
12. Guo, C.; Chen, D.; Qing, H.; Dong, S.; Li, G.; Wang, D.; Qian, Y.; Liu, C. Multiple dolomitization and later hydrothermal alteration on the Upper Cambrian-Lower Ordovician carbonates in the northern Tarim Basin, China. *Mar. Pet. Geol.* **2016**, *72*, 295–316. [[CrossRef](#)]
13. Du, Y.; Fan, T.; Machel, H.G.; Gao, Z. Genesis of Upper Cambrian-Lower Ordovician dolomites in the Tahe Oilfield, Tarim Basin, NW China: Several limitations from petrology, geochemistry, and fluid inclusions. *Mar. Pet. Geol.* **2018**, *91*, 43–70. [[CrossRef](#)]

14. Dai, Y.D.; Li, J.Y.; Jiang, X.G.; Zhao, S.C.; Kui, H.; Huang, H.L.; Xiao, Q.Y. Petrography of carbonate rocks from the Permian Maokou formation and their reservoir properties in southern Sichuan Basin. *Chin. J. Geol.* **1978**, *3*.
15. Zhou, L.F. Diagenetic deutero-genetic change in Maokou formation of Permian of well mile no.87 in Dazu county, Sichuan, and its influence on reservoir characteristics. *J. Southwest Pet. Inst.* **1989**, *3*, 2.
16. Chen, M. A discussion of the origin of Yangxin dolomite of Lower Permian in southwest Sichuan. *Acta Sedimentol. Sin.* **1989**, *7*, 45–50.
17. Zhao, X. Structural-burial hydrothermal dolomitization in the Lower Permian carbonate rocks in central Guizhou. *Sediment. Geol. Tethyan Geol.* **1991**, *6*, 41–47.
18. Chen, X.; Wenzhi, Z.; Yinhe, L. Characteristics and exploration strategy of the Middle Permian hydrothermal dolomite in southwestern Sichuan Basin. *Acta Pet. Sin.* **2013**, *34*, 460–466. [[CrossRef](#)]
19. Wang, H.; Hao, S.; Dong, H.; Xuewen, S.; Yi, L.; Xiaoling, Y. Origin and distribution of hydrothermal dolomites of the Middle Permian in the Sichuan Basin. *Nat. Gas Ind.* **2014**, *34*, 25–32. [[CrossRef](#)]
20. Han, X.; Bao, Z.; Xie, S. Origin and Geochemical Characteristics of Dolomites in the Middle Permian Formation, SW Sichuan Basin, China. *Earth Sci.* **2016**, *41*, 167–176. [[CrossRef](#)]
21. Chen, X.; Zhao, W.; Zhang, L. Discovery and exploration significance of structure-controlled hydrothermal dolomites in the Middle Permian of the central Sichuan Basin. *Acta Pet. Sin.* **2012**, *33*, 562–569. [[CrossRef](#)]
22. Liu, C.; Xie, Q.; Wang, G.; Song, Y.; Qi, K. Dolomite origin and its implication for porosity development of the carbonate gas reservoirs in the Upper Permian Changxing Formation of the eastern Sichuan Basin, Southwest China. *J. Nat. Gas Sci. Eng.* **2016**, *35*, 775–797. [[CrossRef](#)]
23. Song, H.; Luo, Z. The study of the basement and deep geological structures of Sichuan Basin, China. *Earthence Front.* **1995**, *1995*, 231–237.
24. Wang, Z.; Zhao, W.; Li, Z.; Jiang, X.; Jun, L. Role of basement faults in gas accumulation of Xujiahe Formation, Sichuan Basin. *Pet. Explor. Dev.* **2008**, *35*, 541–547. [[CrossRef](#)]
25. Guo, Z.; Deng, K.; Han, Y. *Formation and Evolution of the Sichuan Basin*; Geological Publishing House: Beijing, China, 1996.
26. Chen, Z. Gas exploration in Sinian Dengying Formation, Sichuan Basin. *China Pet. Explor.* **2010**, *15*, 1–14, 18. [[CrossRef](#)]
27. Mei, Q.; He, D.; Wen, Z.; Li, Y.; Li, J. Geologic structure and tectonic evolution of Leshan-Longnvsi paleo-uplift in Sichuan Basin, China. *Acta Pet. Sin.* **2014**, *27*, 1427–1438. [[CrossRef](#)]
28. Mei, Q.; He, D.; Gui, B.; Li, Y.; Li, J.; Li, C. Multiple rifting and its evolution of central Sichuan Basin in the Neoproterozoic-Paleozoic. *Nat. Gas Geosci.* **2016**, *27*, 1427–1438. [[CrossRef](#)]
29. Zhou, J.; Yao, G.; Yang, G.; Gu, M.; Yao, Q.; Jiang, Q.; Yang, L.; Yang, Y. Lithofacies paleogeography and favorable gas exploration zones of Qixia and Maokou Formations in the Sichuan Basin. *Nat. Gas Ind.* **2016**, *36*, 8–15. [[CrossRef](#)]
30. Tan, X.; Luo, B.; Jiang, X.; Liu, H.; Ling, L.I.; Zhang, B.; Zou, J. Controlling Effect of Basement Fault on Changxing Formation Reef in Sichuan Basin. *Geol. Rev.* **2012**, *58*, 277–284. [[CrossRef](#)]
31. Zhu, C.; Xu, M.; Shan, J.; Yuan, Y.; Zhao, Y.; Hu, S. Quantifying the denudations of major tectonic events in Sichuan basin: Constrained by the paleothermal records. *Geol. China* **2009**, *36*, 1268–1277. [[CrossRef](#)]
32. Zhu, C.; Xu, M.; Yuan, Y.; Zhao, Y.; Shan, J.; He, Z.; Tian, Y.; Hu, S. Palaeogeothermal response and record of the effusing of Emeishan basalts in the Sichuan basin. *Chin. Sci. Bull.* **2010**, *55*, 949–956. [[CrossRef](#)]
33. Huang, S.; Li, X.; Huang, K.; Lan, Y.; Jie, L. Authigenic noncarbonate minerals in hydrothermal dolomite of Middle Permian Qixia Formation in the west of Sichuan Basin, China. *J. Chengdu Univ. Technol.* **2012**, *7*, 343–352. [[CrossRef](#)]
34. Dickson, J. Carbonate identification and genesis as revealed by staining. *J. Sediment. Petrol.* **1966**, *36*, 491–505. [[CrossRef](#)]
35. McLennan, S.M. Rare earth elements in sedimentary rocks; influence of provenance and sedimentary processes. *Rev. Mineral. Geochem.* **1989**, *21*, 169–200.
36. Bau, M. Controls on the fractionation of isovalent trace elements in magmatic and aqueous systems: Evidence from Y/Ho, Zr/Hf, and lanthanide tetrad effect. *Contrib. Mineral. Petrol.* **1996**, *123*, 323–333. [[CrossRef](#)]
37. Golyshev, S. Fractionation of stable oxygen and carbon isotopes in carbonate systems. *Geokhimiya* **1981**, *10*, 1427–1441.

38. Zheng, Y. Oxygen isotope fractionation in carbonate and sulfate minerals. *Geochem. J.* **1999**, *33*, 109–126. [[CrossRef](#)]
39. Coplen, T.B.; Kendall, C.; Hoppfe, J. Comparison of stable isotope reference samples. *Nature* **1983**, *302*, 236. [[CrossRef](#)]
40. Lu, Z.; Chen, H.H.; Qing, H.R.; Chi, G.X.; Chen, Q.L.; You, D.H.; Yin, H.; Zhang, Y.S. Petrography, fluid inclusion and isotope studies in Ordovician carbonate reservoirs in the Shunnan area, Tarim basin, NW China: Implications for the nature and timing of silicification. *Sediment. Geol.* **2017**, *359*, 29–43. [[CrossRef](#)]
41. Goldstein, R.H.; Reynolds, T.J. *Fluid Inclusion Microthermometry*; Special Publications of Society for Sedimentary Geology (SEPM): Broken Arrow, OK, USA, 1994; Chapter 7.
42. Chi, G.; Lu, H. Validation and representation of fluid inclusion microthermometric data using the fluid inclusion assemblage (FIA) concept. *Acta Petrol. Sin.* **2008**, *24*, 1945–1953.
43. Steele-MacInnis, M.; Bodnar, R.; Naden, J. Numerical model to determine the composition of H<sub>2</sub>O–NaCl–CaCl<sub>2</sub> fluid inclusions based on microthermometric and microanalytical data. *Geochim. Cosmochim. Acta* **2011**, *75*, 21–40. [[CrossRef](#)]
44. Chi, G. Equations for calculation of NaCl/(NaCl + CaCl<sub>2</sub>) ratios and salinities from hydrohalite-melting and ice-melting temperatures in the H<sub>2</sub>O–NaCl–CaCl<sub>2</sub> system. *Acta Petrol. Sin.* **2007**, *23*, 33–37.
45. Roedder, E. Fluids in salt. *Am. Mineral.* **1984**, *69*, 413–439.
46. Allan, J.R.; Wiggins, W. *Dolomite Reservoirs: Geochemical Techniques for Evaluating Origin and Distribution*; American Association of Petroleum Geologists: Tulsa, OK, USA, 1993.
47. McArthur, J.M.; Howarth, R.J.; Bailey, T.R. Strontium Isotope Stratigraphy: LOWESS Version 3: Best Fit to the Marine Sr-Isotope Curve for 0–509 Ma and Accompanying Look-up Table for Deriving Numerical Age. *J. Geol.* **2001**, *109*, 155–170. [[CrossRef](#)]
48. Nothdurft, L.D.; Webb, G.E.; Kamber, B.S. Rare earth element geochemistry of Late Devonian reefal carbonates, Canning Basin, Western Australia: Confirmation of a seawater REE proxy in ancient limestones. *Geochim. Cosmochim. Acta* **2004**, *68*, 263–283. [[CrossRef](#)]
49. Gregg, J.M.; Sibley, D.F. Epigenetic dolomitization and the origin of xenotopic dolomite texture. *J. Sediment. Petrol.* **1984**, *54*. [[CrossRef](#)]
50. Sibley, D.F.; Gregg, J.M. Classification of dolomite rock textures. *J. Sediment. Petrol.* **1987**, *57*, 967–975. [[CrossRef](#)]
51. Gregg, J.M.; Bish, D.L.; Kaczmarek, S.E.; Machel, H.G. Mineralogy, nucleation and growth of dolomite in the laboratory and sedimentary environment: A review. *Sedimentology* **2015**, *62*, 1749–1769. [[CrossRef](#)]
52. Machel, H.G. Concepts and models of dolomitization: A critical reappraisal. *Geol. Soc. Lond. Spec. Publ.* **2004**, *235*, 7–63. [[CrossRef](#)]
53. Huang, S. A study on carbon and strontium isotopes of Late Paleozoic carbonate rocks in the Upper Yangtze Platform. *Acta Geol. Sin.* **1997**, *1*, 45–53.
54. Popp, B.; Anderson, T.; Sandberg, P. Brachiopods as indicators of original isotopic compositions in some Paleozoic limestones. *Geol. Soc. Am. Bull.* **1986**, *97*, 1262–1269. [[CrossRef](#)]
55. Peryt, T.; Magaritz, M. Genesis of evaporite-associated platform dolomites: Case study of the Main Dolomite (Zechstein, Upper Permian), Leba elevation, northern Poland. *Sedimentology* **1990**, *37*, 745–761. [[CrossRef](#)]
56. Land, L.S. The isotopic and trace element geochemistry of dolomite: The state of the art. *Spec. Publ. Soc. Sediment. Geol. (SEPM)* **1980**, *28*, 87–110.
57. Qing, H.; Bosence, D.W.; Rose, E.P. Dolomitization by penesaline sea water in Early Jurassic peritidal platform carbonates, Gibraltar, western Mediterranean. *Sedimentology* **2001**, *48*, 153–163. [[CrossRef](#)]
58. McKerrow, W.S.; Scotese, C.R. *Palaeozoic Palaeogeography and Biogeography*; Geological Society: London, UK, 1990; Volume 12.
59. Shields, M.J.; Brady, P.V. Mass balance and fluid flow constraints on regional-scale dolomitization, Late Devonian, Western Canada Sedimentary Basin. *Bull. Can. Pet. Geol.* **1995**, *43*, 371–392.
60. Potma, K.; Weissenberger, J.A.; Wong, P.K.; Gilhooly, M.G. Toward a sequence stratigraphic framework for the Frasnian of the Western Canada Basin. *Bull. Can. Pet. Geol.* **2001**, *49*, 37–85. [[CrossRef](#)]
61. Qing, H.; Mountjoy, E.W. Formation of coarsely crystalline, hydrothermal dolomite reservoirs in the Presqu'île Barrier, Western Canada Sedimentary Basin. *AAPG Bull.* **1994**, *78*, 55–77.
62. Warren, J. Dolomite: Occurrence, evolution and economically important associations. *Earth-Sci. Rev.* **2000**, *52*, 1–81. [[CrossRef](#)]

63. Machel, H.G.; Buschkuhle, B.E. Diagenesis of the Devonian Southesk-Cairn Carbonate Complex, Alberta, Canada: Marine cementation, burial dolomitization, thermochemical sulfate reduction, anhydritization, and squeeze fluid flow. *J. Sediment. Res.* **2008**, *78*, 366–389. [[CrossRef](#)]
64. Aulstead, K.L.; Spencer, R. Diagenesis of the Keg River Formation, northwestern Alberta: Fluid inclusion evidence. *Bull. Can. Pet. Geol.* **1985**, *33*, 167–183.
65. Lavoie, D.; Chi, G.; Brennan-Alpert, P.; Desrochers, A.; Bertrand, R. Hydrothermal dolomitization in the Lower Ordovician Romaine Formation of the Anticosti Basin: Significance for hydrocarbon exploration. *Bull. Can. Pet. Geol.* **2005**, *53*, 454–471. [[CrossRef](#)]
66. Frimmel, H.E. Trace element distribution in Neoproterozoic carbonates as palaeoenvironmental indicator. *Chem. Geol.* **2009**, *258*, 338–353. [[CrossRef](#)]
67. Bau, M. Rare-earth element mobility during hydrothermal and metamorphic fluid-rock interaction and the significance of the oxidation state of europium. *Chem. Geol.* **1991**, *93*, 219–230. [[CrossRef](#)]
68. Kučera, J.; Cempírek, J.; Dolníček, Z.; Muchez, P.; Prochaska, W. Rare earth elements and yttrium geochemistry of dolomite from post-Variscan vein-type mineralization of the Nížký Jeseník and Upper Silesian Basins, Czech Republic. *J. Geochem. Explor.* **2009**, *103*, 69–79. [[CrossRef](#)]
69. Lind, I.; Berger, W.; Kroenke, L. Stylolites in chalk from leg 130, Ontong Java Plateau. In Proceedings of Proceedings of the Ocean Drilling Program. *Sci. Results* **1993**, *130*, 445–451.
70. Dunnington, H. Aspects of Diagenesis and Shape Change in Stylolitic Limestone Reservoirs. In *7th World Petroleum Congress*; World Petroleum Congress: London, UK, 1967.
71. Buxton, T.M.; Sibley, D.F. Pressure solution features in a shallow buried limestone. *J. Sediment. Petrol.* **1981**, *51*, 19–26. [[CrossRef](#)]
72. White, D.E. Thermal waters of volcanic origin. *Geol. Soc. Am. Bull.* **1957**, *68*, 1637–1658. [[CrossRef](#)]
73. Xu, Y.; He, B.; Luo, Z.; Liu, H. Study on mantle plume and large igneous provinces in China: An overview and perspectives. *Bull. Mineral. Petrol. Geochem.* **2013**, *32*, 25–39. [[CrossRef](#)]
74. He, B. Research Progress on Some Issues on the Emeishan Large Igneous Province. *Adv. Earth Sci.* **2016**, *31*, 23–42. [[CrossRef](#)]
75. Zhang, C.J.; Liu, J.D.; Liu, X.F.; Yang, Z.X.; Liu, Y.G.; Wu, D.C. Primary discussion on ore-forming effect of Emei igneous province. *J. Mineral. Petrol.* **2004**, *24*, 5F9. [[CrossRef](#)]
76. Wang, Y.; Yu, X.; Yang, Y.; Zhang, J. Applications of fluid inclusions in the study of Paleo geotemperature in Sichuan Basin. *Earth Sci. J. China Univ. Geosci.* **1998**. [[CrossRef](#)]
77. Huang, S.J.; Hu, Z.W.; Zhong, Y.J.; Huang, K.K.; Li, X.N. Saddle dolomite in Permian-Triassic carbonate rocks and sandstones of Sichuan Basin: petrology, formation temperature and palaeofluids. *J. Chengdu Univ. Technol.* **2015**, *42*, 129–148.
78. Jiang, Q.; Hu, S.; Wang, Z.; Wang, T.; Li, Q.; Zhai, X. Genesis of medium-macro-crystalline dolomite in the Middle Permian of Sichuan Basin. *Oil Gas Geol.* **2014**, *35*, 503–510. [[CrossRef](#)]

